Structural monitoring of a church influenced by mining settlements using spaceborne remote sensing

by

Student Name	Student Number
Raymond Brouwers	4489160

supervised by

Dr. Giorgia Giardina
Prof. Dr. Max Hendriks
Dominika Malinowska
Dr. Pietro Milillo
Dr. Anjali Mehrotra

April, 2022

Faculty of Civil Engineering and Geosciences

Abstract

Structural health monitoring of buildings is useful for a few reasons. It provides information on the usage and cause of damage to a building. This can result in targeted maintenance or allow for potential improvements.

Traditionally, a building can be monitored by installing sensors during construction or maintenance work. These can be strain gauges, inertial measurement units or surveying equipment. However, not all buildings have such sensors installed due to lack of space or the cost of the equipment. To overcome this, a spaceborne technique shows potential, namely multi-temporal interferometric synthetic aperture radar (MT-InSAR). This technique has already been applied to monitor damage to sections of buildings or large structures, for instance facades or deformations of bridges. In the context of entire buildings, the result of an MT-InSAR analysis has not yet been paired with a computational model. This is mainly due to the relatively small scale of a building and low spatial density of the displacement data.

This thesis integrates remote sensing data, acquiring displacements due to mining, with a computational structural finite element model of a church structure. The displacements have been interpolated using MT-InSAR data, which contains projections of nonlinear displacements in vertical and West-East directions. The interpolation has been performed using two techniques. The first is Ordinary Kriging, which is used to obtain a general insight into the deformations and the shape of the deformed region near the church. The second uses the least squares method to fit polynomial shape functions. The resulting displacements of the least squares analysis have been integrated into a nonlinear structural finite element model. The structural model consists of a soil-structure interaction model and nonlinear material properties, and is used to assess crack propagation.

Integrating remote sensing with computational modelling, shows potential in providing a monitoring technique for buildings. The interpolation method can be used to obtain displacements at a building, even when the spatial density of the InSAR analysis is limited. The main limitation is the information on the horizontal displacements obtained by the InSAR technique, where the displacement along the North-South is unknown. Furthermore, the structure and integration can then be performed using a finite element model, which can follow crack propagation and account for soil-structure interaction.

Acknowledgements

This thesis has been quite a personal challenge for me. It started in the midst of the corona pandemic. Finding solutions to the problem posed by the thesis encouraged me the most. The writing, however, proved to be a whole other issue, often at times resulting in a struggle to find the motivation to complete my work. I am extremely grateful to my family, the committee and close friends for helping me overcome my procrastination and close the chapter on my master's degree. Over the course of completing my thesis, I've not only learned valuable skills pertaining to completing a thesis, but I've also gotten to know myself better.

I would like the thank my parents, for lending a listening ear and helping me proof read most of my writing. My dad with who I could bounce off my ideas and my mom was always there even when I was just rambling on and on. Thank you to my aunt, Karen, who tried to keep me from wavering and always showed interest in how I was doing.

My friends, who believed in my ability and aspects of my work when I struggled myself. Hearing about their thesis experiences definitely helped me in realizing I'm not alone. They often brought a smile to my face when things got tough and reminded me that everyone has their fair share of hindrances. A special thank you to Philippe for helping me with the practical aspects of the thesis; Mikki for providing me with useful tips relating to writing; and Kunal for aiding me in setting up my defense.

Thank you to my committee, especially Giorgia, Dominika and Max. I would like to thank you for always making an effort to be present during meetings. Also for not showing frustration and instead compassion when things got hard. Giorgia who provided me with a lot of constructive criticism, most noticeable during the final stages of writing. Dominika who helped out a tremendous amount, and with whom this thesis topic would otherwise not have been possible. She provided me with useful tips along the way and acquired the data required to initiate the thesis. In addition, she managed to obtain information and translated documents related to the structure analysed in my work.

Contents

1 Introduction

Structures over the years can suffer from differential displacements due to changes in the supporting soil layers. This can lead to unwanted cracks, high repair costs or even failure. Structural health monitoring (SHM) provides a means of detecting and assessing the severity of the damage in those situations. It lends insight into the usage and degradation of a structure. In addition, it can detect damage early and identify which components are most prone to failure. The latter provides suggestions for improvement or can aid during maintenance operations. This minimises downtime and increases the longevity of the building [Balageas et al., 2010].

1.1 Problem statement

To make health monitoring possible, data must be acquired. This can come from various sources. For some bridges and buildings, sensors are installed either during construction or maintenance. However, the bulk of existing structures lack these observation sensors due to cost or the lack of time or space. For instance, the funding to set up monitoring equipment may not be present while damage is undetectable or a building is enclosed by other structures [Yang et al., 2016]. A potential solution to the lack of data is MT-InSAR (Multi-temporal Interferometric Synthetic Aperture Radar), a spaceborne technique able to obtain deformations over large areas, with an accuracy up to a few millimetres [Ferretti et al., 2001]. InSAR has been used in other research to evaluate the damage to buildings, bridges and dams [Giardina et al., 2019, Selvakumaran et al., 2020, Corsetti et al., 2018]. It has also been used in a general context to assess the damage of old heritage structures countrywide [Drougkas et al., 2020b]. The gap is the research on integrating a computational model of a building with deformations obtained from an MT-InSAR analysis. The main problem is obtaining enough displacement observations points at the buildings. This is a consequence of the low spatial density of an MT-InSAR analysis.

In some instances, such as local mining, landslides or soil consolidation over large regions (greater than a 400 m radius), it is believed that interpolation can be used to solve for the low spatial density. Underground mining, for example, coal mining near a building, often results in surface deformations. These vertical or horizontal deformations can pose a risk to nearby structures. Specifically, differential settlements cause concern [Altun et al., 2010]. This thesis aims to establish an approach to monitor a church structure influenced by mining settlements. The problem is split into two components. The first is obtaining more deformations at the building using interpolation and the results of an MT-InSAR analysis. The second is to incorporate those deformations in a structural model and estimate the crack-width to monitor the damage.

1.2 Research questions

The main objective of this thesis is to integrate deformations obtained using satellite data and computational modelling of buildings. Therefore, the main research question is, "How to monitor the structural response of a building influenced by mining deformations using remote sensing?". During this process, the following sub-questions are addressed.

- "How to obtain deformations from an MT-InSAR analysis for integration in a structural model?"
- "How to integrate the displacements and model a building?"
- "What are the most important modelling criteria for determining the crack-width in the structural response?"

1.3 Methodology

The thesis is divided into three main components to resolve the research questions. The first one focuses on obtaining displacements at the church. MT-InSAR obtains deformations at specific locations, known as persistent scatters, of which a large amount are assumed to be positioned on nearby structures. The spatial density of the analysis is too low to evaluate differential deformations at a single building. To overcome this, the deformations are interpolated, and general remarks are made on the applicability of the remote sensing data. The second part concentrates on establishing a nonlinear structural finite element model. In addition, different element and analysis types within the FEM approach are reflected. The third and final component is the actual integration and assessment of the structural damage.

The building analysed is a church located in Jastrzębie Zdrój, Poland. The structure was built between 1796 and 1801, and can be seen in Figure 1. The church is believed to be affected by mining deformations. Over the years, the church has undergone multiple renovations, with recent ones being funded by a mining cooperation. The mining cooperation has an active mining region at the church called Borynia, as shown in Figure 2. It was launched in late 1971 and has, when last checked, obtained a contract to continue mining from 2017 till the end of 2025. It is currently part of Jastrzębska Spółka Węglowa SA and is mining at depths greater than 700 m below the surface [Institute, 2020, Wikipedia, 2020].

Two techniques have been used to interpolate the displacement data from a nonlinear MT-InSAR (Multi-temporal Interferometric Synthetic Aperture Radar) analysis. The first uses Ordinary Kriging, a statistical unbiased interpolation method. This is done to gain a general insight into the deformations surrounding the structure and to establish the spatial covariance. The second uses the least squares method with a selected polynomial shape function, of which the coefficients are recomputed at each observation time.

Figure 1: Picture of the church. [Google, 2012]

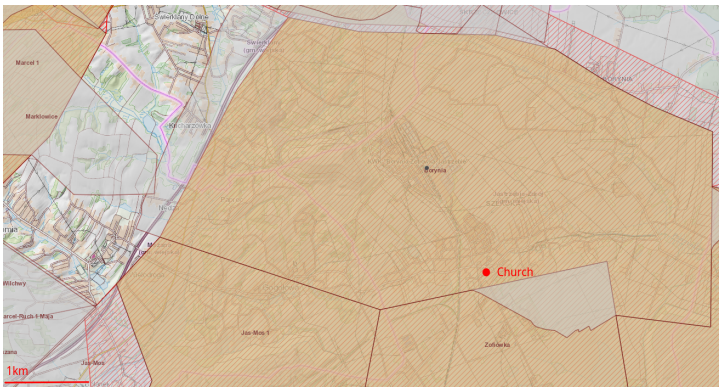

Figure 2: Mining region Borynia and church in Jastrzębie Zdrój, Poland. [Institute, 2020]

Only the latter is integrated with the structural model. The approach avoids including a too-large region of influence while maintaining enough persistent scatters[1] to perform the interpolation.

At the same time, the structural model of the church has been established. This has been done by interpreting existing drawings, images and information related to the church. Next, the structurally critical components have been identified and modelled using DIANA[2]. For the model, nonlinear masonry material behaviour has been included to account for the development and propagation of cracks. The masonry is assumed to be homogeneous and behave isotropic linear elastic till the point of crack formation, after which the stress decreases as the strain increases. Furthermore, a soil-structure interaction (SSI) model has been assumed to allow for integrating the deformations and modelling of the structure. This model uses interface elements with a fixed linear stiffness.

After establishing the deformation and structural model, the final damage assessment can be performed. This evaluation only considers deformations occurring over 6 years due to a limitation in the availability of the satellite data. In addition, the sensitivity to variations in material or soil properties are discussed, and the variations in the deformations are made. The result is that the effect of the interpolated deformations is evaluated, and the most important aspects of both models are identified.

1.4 Thesis outline

The document is divided into four main sections. The first provides a brief background on the specific technique used to obtain deformations. The second section specifies how the deformations were acquired and further processed to obtain input data for the structural model. Next, a more in-depth structural description of the church has been provided and modelled. Then finally, the results of the model integration and a sensitivity analysis are presented.

[1] Persistent scatters are the points at which the deformations are known.
[2] DIANA FEA is a finite-element analysis software.

2 Background on remote sensing

To obtain the displacements Multi-Temporal Interferometric Synthetic Aperture Radar (MT-InSAR) has been used. The method provides an inexpensive and accurate means of monitoring deformations on a large scale. In addition, this technique can usually obtain deformations with an accuracy of up to a few millimetres [Ferretti et al., 2001]. This subsection gives a brief glance at the technique and the limitations involved. To do this, an introduction is provided into orbits, Synthetic Aperture Radar and how it can be used to obtain displacements.

2.1 Satellite orbits

Orbits refer to a path followed by bodies in space, of which some are considered indefinite and repetitive. A repetitive orbit is characterised by an orbital period, which refers to the time required to repeat the orbit. This time depends on the altitude of the orbit and gravitational pull. The inclination of an orbit refers to the angle a path makes with respect to an orbit travelling around the equator moving in the same direction as the rotation of the Earth. Polar orbits are at roughly a 90-degree incline, passing the Northern and Southern hemispheres. This type of orbit can deviate with 20 to 30 degrees. The main advantage of an inclined orbit such as a polar orbit is that the surface location over which it passes can vary over time, depending on the orbital period and the Earth's rotation cycle. In the case of an imaging satellite, such as the ones used for MT-InSAR, a specific polar known as a Sun-synchronous orbit (SSO) is most favourable, shown in Figure 3. [ESA, 2020]

A sun-synchronous orbit recesses similar to a gyroscope. This effect is synchronised with the Earth's movement around the sun. By doing so, the satellite is able to sustain a near-identical angle of illuminance on repeat passes. Two main benefits stem from this. The first is that it makes it easier to design the satellite regarding the power and cooling systems. The second relates to radar and optical satellites. In this case, fluctuations in lighting and thermal conditionals in the day cycle are minimised, particularly useful in the case of thermal expansion. Polar orbits (and SSOs) are either ascending or descending, this term refers to which pole they are currently travelling towards. An ascending orbit is heading from South to North, whilst a descending orbit is moving from North to South. [Doody, 2022]

2.2 Interferometric synthetic-aperture radar

Synthetic-Aperture Radar (SAR) satellite is an active remote sensing method. The satellite emits pulses and receives them upon reflection. It uses its motion in space to create a synthetically larger radar antenna to improve the spatial resolution. In this case, the wavelength of the pulses can penetrate clouds, or even vegetation and snow, as illustrated in Figure 4. For this thesis, the method can obtain two key pieces of

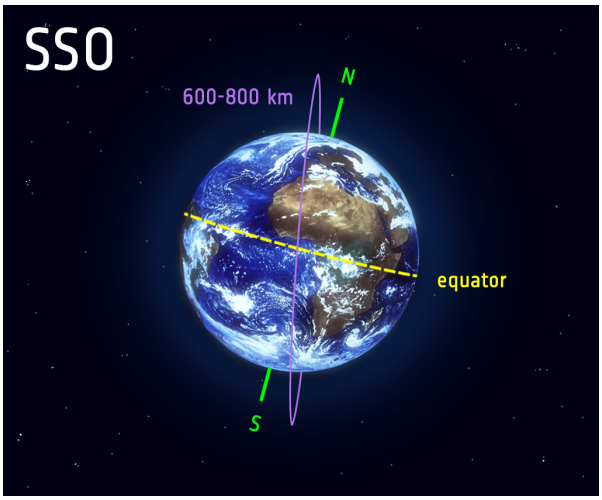

Figure 3: This figure illustrates a sun-synchronous orbit (SSO) that is approximately 600 to 800 km from the surface of the Earth at an incline of roughly 98 degrees. This is a polar orbit which is slightly retrograde, which implies an object would travel in the opposite direction of the Earth's rotation. [ESA, 2020]

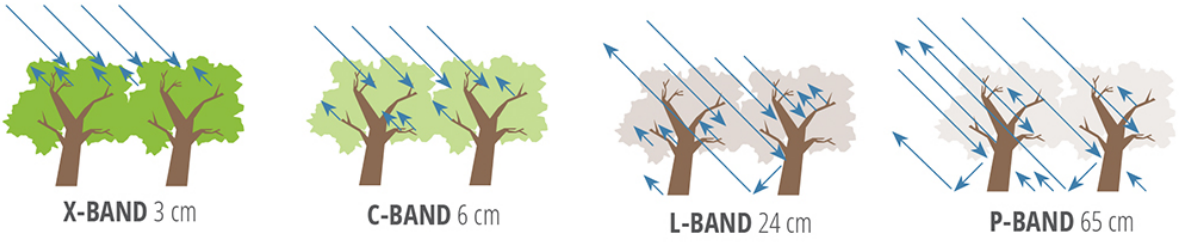

Figure 4: This Figure illustrates the effect of different wavelengths used in SAR and how they reflect or penetrate vegetation. [Herndon et al., 2021]

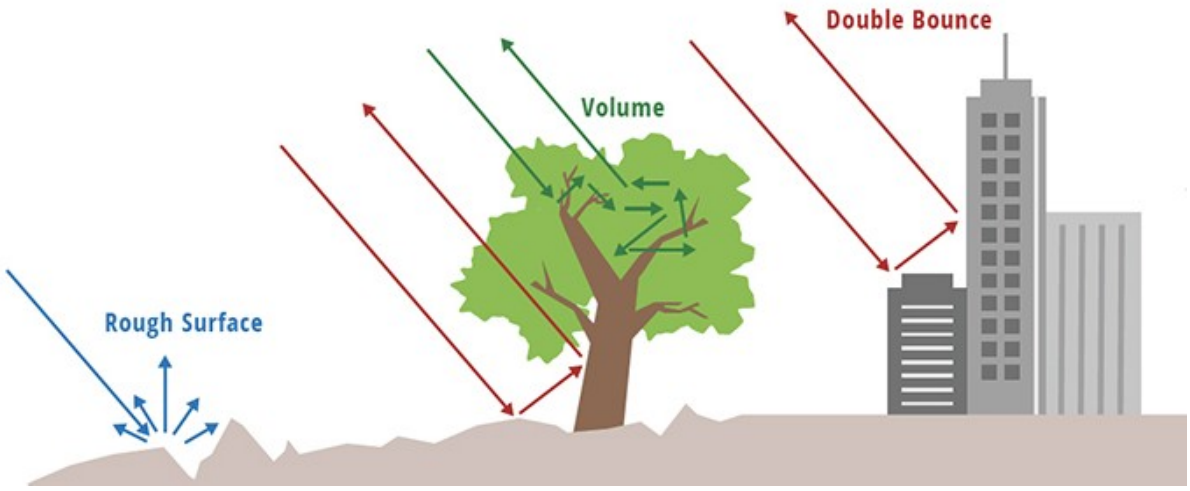

Figure 5: This figure illustrates the reflectivity of SAR on different surfaces. To obtain an observation, the signal should return in the same direction as it originated from. In this case, both the aspects of not returning and double bounce scattering are illustrated; neither are favourable when considering the change in distance travelled. [Herndon et al., 2021]

information upon return. The first is the amplitude which provides a measure for the signal strength. The second is the phase of the returned signal. The amplitude is very dependent on the surface type, of which an illustration is shown in Figure 5. For instance, very flat mirror-like surfaces, such as calm water, will reflect in a different direction than the receiving radar. This makes SAR inappropriate for observing water bodies. Other surfaces can absorb or keep reflecting internally. This is known as volume reflection and is common for dense vegetation. [Herndon et al., 2021]

For observing displacements over time, having a single satellite pass is not very useful. However, the phase difference between two images can be taken on a repeat pass. This is referred to as an interferogram, an example of which is shown in Figure 6. Interferograms can be useful to get global insight into the deformation difference on a large scale, provided the duration between the SAR images is relatively short (a few days). As the time between acquisitions increases or more detailed points would like to be observed, it starts to fall short. In general, the phase change is dependant on multiple factors besides deformations. A few examples of this are phase ambiguity, atmospheric delays and temporal changes [Perissin, 2016]. To solve some of these, Multi-Temporal Interferometric Synthetic Aperture Radar (MT-InSAR) is introduced. MT-InSAR is a technique using of a stack created from multiple interferograms acquired over an extended observation period. Pixels that show consistent radar reflection over time are identified as Persistent Scatters (PSs). Persistent scatters are often radar targets smaller than the resolution cell, and they are characterised by a temporal coherence coefficient situated between 0 and 1. This coherence can serve as a good indicator of how reliable a point is, a higher value is more favourable. During an MT-InSAR analysis a reference point must be selected. This point should remain motionless during the entire observation time to reduce the estimation errors on the remaining PSs.

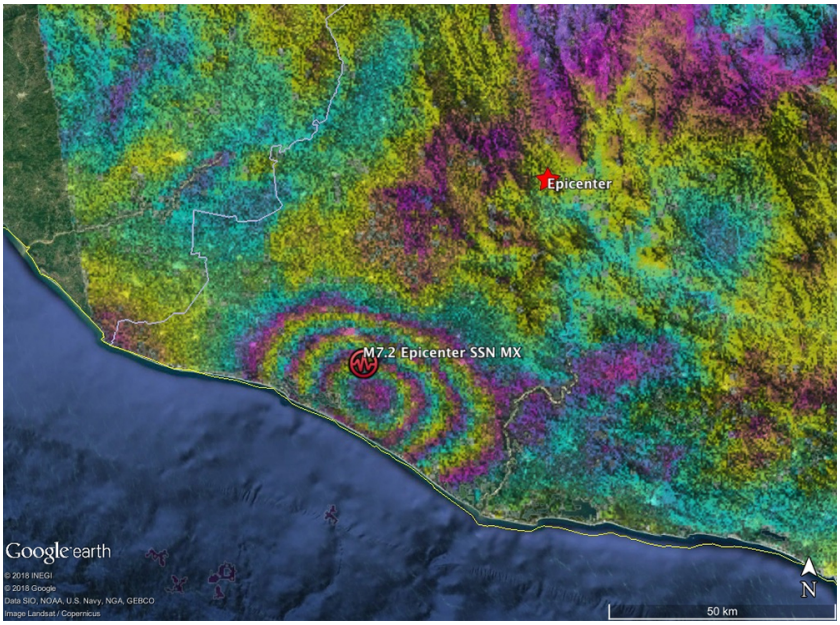

Figure 6: Interferogram from Sentinel-1 SAR data acquired at 2018-02-17 and 2018-02-05 shows earthquake fault slip on a subduction thrust fault causing up to 40 *cm* of uplift of the ground surface. The motion has been contoured with 9 cm colour contours, also known as fringes. Credit: NASA Disasters Program.

The satellites observe line-of-sight distance changes. However, it is more useful to know vertical and horizontal motion when considering structures. Fortunately, the vertical and West-East motion can be decomposed due to the nature of a polar orbit and the incident angle of the satellite[3]. This decomposition can be performed when combining both ascending and descending passes of the SAR satellites, as shown in Figure 7 or Equation 1. To decompose the line-of-sight displacements, the point must be observed during both ascending and descending passes. Two approaches can be taken to perform the decomposition. The first uses interpolation, to create a set of points at which the decomposition is evaluated. The second is to assume the displacements are identical at points in close proximity to each other. It is essential when performing the decomposition that the reference points are stationary, as there would otherwise be a bias on the entire decomposition process.

$$\begin{aligned} d_{East} &= \frac{1}{2}\left(\frac{d_{dsc}}{sin(\theta_{dsc})} - \frac{d_{asc}}{sin(\theta_{asc})}\right) \\ d_{Up} &= \frac{1}{2}\left(\frac{d_{dsc}}{cos(\theta_{dsc})} + \frac{d_{asc}}{cos(\theta_{asc})}\right) \end{aligned} \tag{1}$$

However, a disadvantage of InSAR is that no motion along the orbit can be observed, as it is perpendicular to the line-of-sight observations. This implies that the magnitude of a horizontal displacement on the surface can only be estimated by a single component.

[3]An angle made with the normal to the surface. In this case also perpendicular to the flight path.

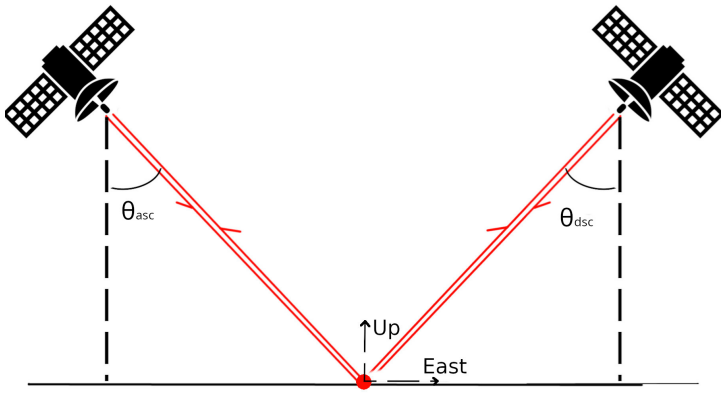

Figure 7: Horizontal and vertical decomposition using ascending and descending flight paths. The ascending orbit (travelling from South to North) is the one on the left, descending (travelling from North to South) is on the right. The incident angle is shown with θ and refers to the angle at which the radar is oriented, which can never be zero. When combining the line-of-sight displacements (changes observed in the length of the red lines), the vertical and horizontal (West-East) displacements can be decomposed.

3 Deformations

This section focuses on how the deformations for the structural model are obtained, after acquiring the data from an MT-InSAR analysis.

In this case, the soil deformations surrounding the church structure are the result of coal mining. The mining occurs about 700 m below the surface and is believed to influence an area the size of several square kilometres, within which the church is situated. Furthermore, it is assumed that the mining deformations are continuous and gradually changing over a distance of a few meters. There are two problems with directly using the data of the MT-InSAR analysis. The first and main problem is the spatial density of the data. With an approximate footprint of 30 m by 15 m, the church only contains a single persistent scatter. To avoid creating a large finite element model for modelling the soil, more deformations at the church are required. The second problem is the origin of the persistent scatters (PSs). In the analysed data, the PSs can be from any arbitrary object, without a distinction being established between a rooftop or the pavement, for instance. This implies that even if the accuracy of an individual persistent scatter is high, it would likely deviate from the soil deformations at that location. This is because the motion would have been transformed by the reflecting structure or object. A solution to these problems is believed to be interpolation. Interpolation permits estimates to be computed at various locations within the church and can identify a trend using multiple PSs.

In this section, two techniques have been applied to interpolate the displacements. Both perform spatial interpolation on the cumulative displacement at discrete observation times. The first one is Ordinary Kriging which uses persistent scatters located within a 750 - 800 m radius from the church, referred to as the "large-scale model". The second establishes the best fit to a polynomial shape function using least squares (LSQ) and includes PSs within a 360 m wide square region, referred to as the "local-scale model". Ordinary Kriging provides an unbiased linear interpolation method and has been used in other cases of mining-induced displacements [Chen et al., 2020]. The method has few assumptions related to the data it is applied on, and it is robust enough to allow some deviations [Oliver and Webster, 2014]. Kriging, in general, assumes a stationary process and a constant variogram[4]. Least squares with the polynomials has been chosen to obtain a better local estimate than the larger-scale model, specifically at the structure. LSQ requires less persistent scatters than Kriging, for which it is recommended to have at least 150 points when establishing the variograms. Kriging also tends to smoothen the profile on a small region [Oliver and Webster, 2014]. In addition, with the polynomial shape function, one can apply a Savitzky-Golay filter[5] on the coefficients across the observation times to reduce the high-frequency deformations fluctuations.

$$f_N(x,y) = \sum_{i=0}^{N} \sum_{j=0}^{N-i} c_{ij} x^i y^j \text{ with N being the polynomial order} \tag{2}$$

[4] A function describing the spatial covariance based on the distance between points.
[5] A low-degree polynomial fitting to successive sub-sets using linear least squares.

This section consists of four main sections. The first contains a brief explanation of the initial input data that is acquired using MT-InSAR. This is followed by two sections elaborating on the results of the interpolation models. The last subsection discusses the results.

3.1 Data acquisition

Dominika Malinowska has provided both the horizontal and vertical deformation data over time. The data originates from 2 satellites, Sentinel-1A and Sentinel-1B, recorded between December 2014 and December 2020. Initially, images were acquired every 12 or 24 days by 1A, and then later, with the launch of 1B in 2016, this was reduced to every 6 or 12 days. The line-of-sight displacements have been acquired by performing a Multi-Temporal Interferometric Synthetic Aperture Radar (MT-InSAR) analysis using SARPROZ [SARPROZ, 2021]. The displacement model was assumed to be nonlinear. In both ascending and descending sets, a filter requiring a temporal coherence greater than 0.7 was implemented, which should aid in obtaining reliable displacement values. The result of these analysis is two CSV files containing the estimated coordinates and cumulative line-of-sight displacements at each timestamp. The error estimation of this data is not included, which subsequently inhibits providing a confidence interval during the interpolation schemes in subsections 3.2 and 3.3.

Both ascending and descending datasets have been used to decompose the displacements into their horizontal (West-East) and vertical components. For the decomposition points, the closest unique set of point pairs (ascending and descending) are assumed to be at the same location, provided the distance is not greater than 10 m for each pair. When performing an MT-InSAR analysis a reference point has to be chosen. In this case, the reference point is not the same. However, they are located approximately 52 m from each other and are in a region assumed to be unaffected by the mining.

Figures 8 and 9 show the accumulated displacements over the observation period of 2178 days. The figures show significant horizontal and vertical displacement, passing an absolute difference of 80 mm surrounding the church. The church appears to be located between two regions more affected by the mining, placing it on a slope both regarding the horizontal and vertical displacements.

3.2 Large-scale model

For the large-scale model, Ordinary Kriging has been applied. Ordinary Kriging uses weight-based linear interpolation, where the weights are determined using a variogram model. A variogram describes the relation between the spatial covariance and the distance between points. The input data contains an array of persistent scatters paired with a sub-array of cumulative displacements at multiple timestamps throughout the six-year observation period.

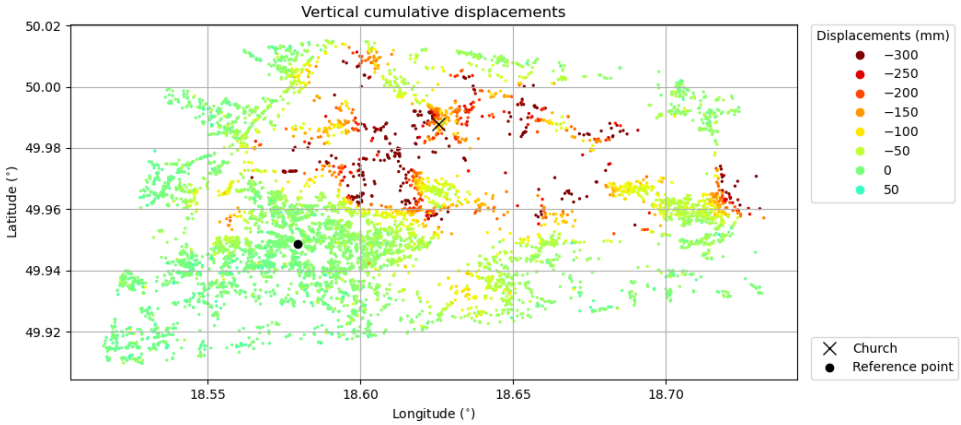

Figure 8: Cumulative vertical displacements after 2178 days, obtained after performing an MT-InSAR analysis and component decomposition. An upwards motion is positive. The church and reference point are located at $49.99°, 18.63°$ and $49.95°, 18.58°$ respectively. The majority of the points appear to be settling. The church seems to be on a slope and settling less than regions to its lower left and right.

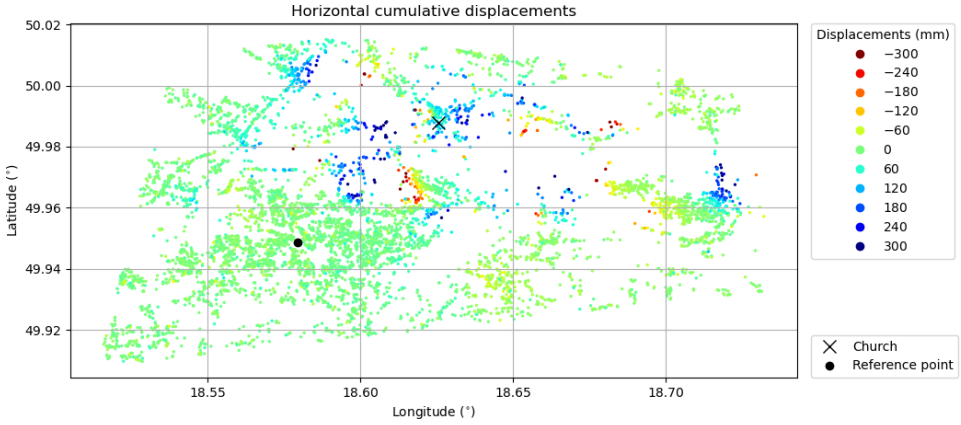

Figure 9: Cumulative horizontal displacements after 2178 days, obtained after performing an MT-InSAR analysis and component decomposition. A motion towards the East is positive. The church and reference point are located at $49.99°, 18.63°$ and $49.95°, 18.58°$ respectively. The church is shifting towards the right (East).

For the variogram, a model is selected and parameters have been fitted for each timestamp, as to create an array of variograms, one for each column of the input data. To establish a reliable variogram, it is recommended to include at least 150 observation points [Oliver and Webster, 2014]. The models that have been considered are a Gaussian, exponential, spherical, linear, power and hole-effect model. Upon selecting one, based on what appears the most suitable, least squares has been applied to estimate the parameters. This is done by computing the spatial variance based on the empirical data, at a specified number of lag distances. The number of distances is decided based on the number of observation points and the coefficient count of the model [Oliver and Webster, 2014]. Including too many distances, can result in an unreliable computation. Once the variograms have been fitted, interpolation can be performed and discussed.

3.2.1 Application and results

For the variogram, a Gaussian model appeared to consistently fit both the horizontal and vertical deformation input data best. The number of points included has been determined by considering two things. The first is to include at least 150 points for reliability. The second is to ensure that the variogram model remains consistent with the observation. When including too many points, the Gaussian model is no longer a good fit. Figure 10 shows the effect of different inclusion ranges on the variogram model. For the vertical displacements, an inclusion radius of 800 m has been found to be optimal, resulting in the 160 points, shown in Figure 11. The horizontal displacements includes points within a 750 m radius, containing 154 observation points. Figures 12 and 13 show the variograms of the vertical and horizontal displacements on the date that the greatest differential displacements can be observed at the church. In both, the range over which the variance increases before reaching the sill is approximately 900 m; beyond this distance, a point is no longer considered relevant when interpolating.

Vertical displacements
The vertical displacements have been observed to be the largest settlements are located towards the North-West of the church. Over time the largest deformation gradient at the church rotates from pointing towards North-East to South-East. The deformations surface surrounding the church is curved, with the principle curvature direction remaining near constant over time. This curvature is not constant within the region of the local-scale model, and plays an important role in causing bending cracks in the church. Figures 14 and 16 show the cumulative displacements and curvature when they are believed to be most critical.

Horizontal displacements
The horizontal displacement is approximately linear near the structure, with a slight curvature. This trend remains valid over the observed time span, especially when the peak displacement differences are observed. This is shown in Figure 17, where the

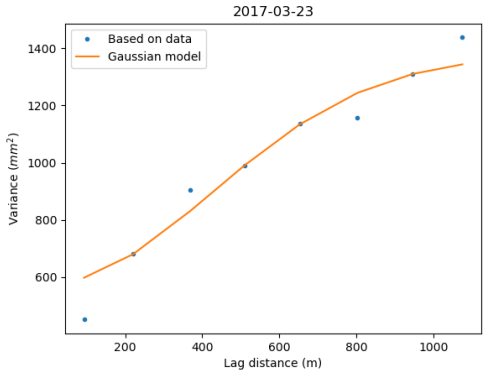

(a) 600 m

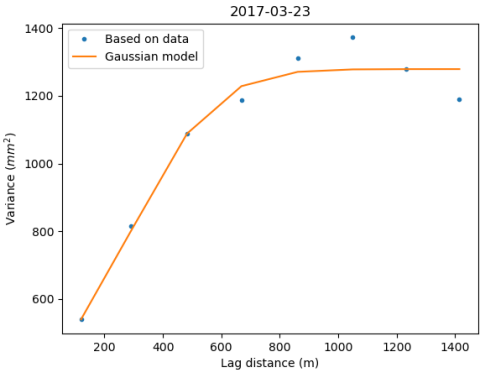

(b) 800 m

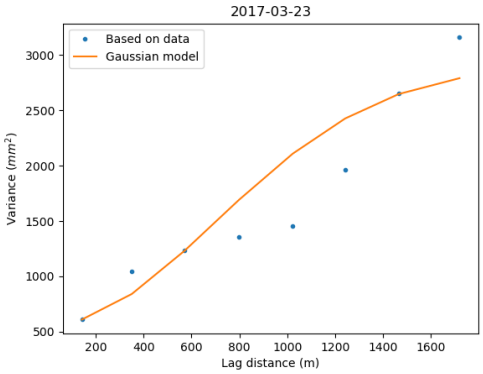

(c) 1000 m

Figure 10: Identical variograms to Figure 12. The only difference is that (a) and (c) are applied at a different inclusion radius to show the difference in the fit of the Gaussian model. Figure (a) doesn't properly reach the sill, horizontal section, which is visible in both (b) and (c). Figure (c) deviates from the shape the Gaussian model can acquire as the lag distance increases towards the end again.

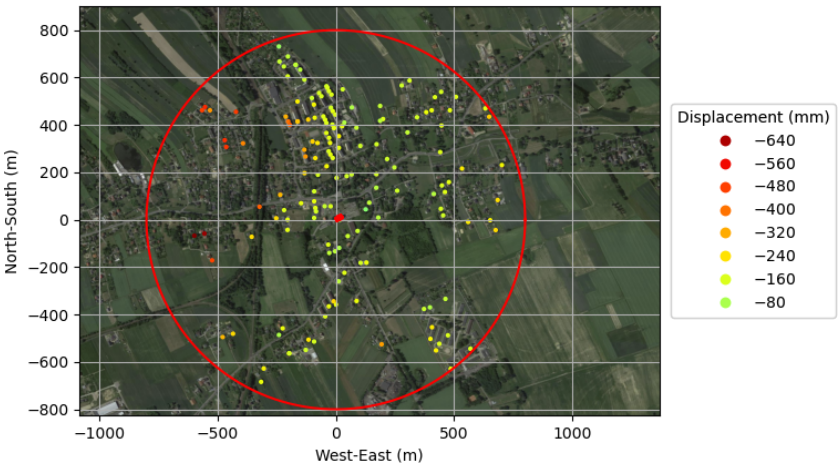

Figure 11: This plot shows the 160 points used in the large-scale interpolation model of the vertical displacements. The inclusion radius is 800 m. The values represent the cumulative vertical displacement from 2014-12-16 till 2020-12-02. The centre is located at the main entrance of the church (plotted in red, at the origin).

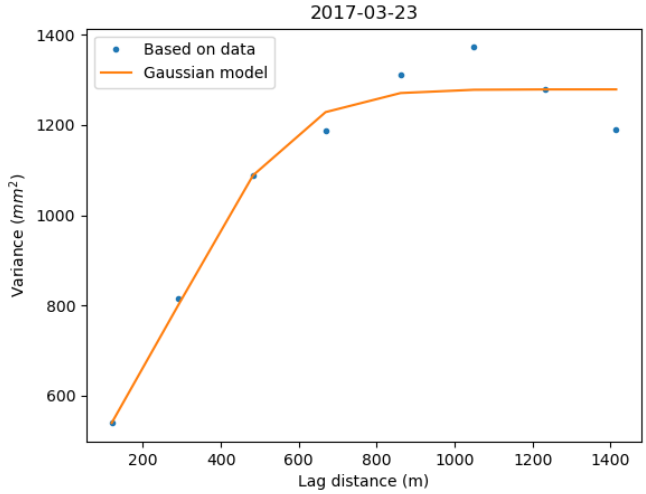

Figure 12: Variogram model used in performing Ordinary Kriging interpolation fitted to the Gaussian model, and calculated using a "soft" L1 norm minimisation scheme. This plot describes the variance of the vertical displacements (y-axis) as a function of lag distance (x-axis) and indicates that displacements are less related as the distance increases. The range lag distance of $\approx$ 900 m indicates the influence region of the mining settlements. The non-zero nugget (value at distance 0) is $\approx 470mm^2$. This is likely caused by the lack of closely spaced points, implying the value is extrapolated, and noise in the observations.

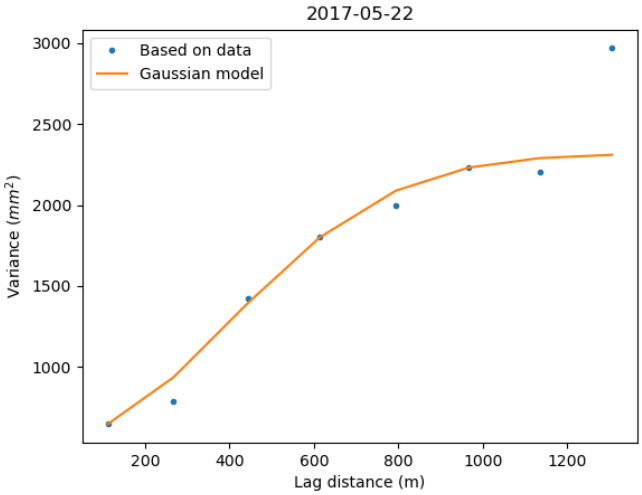

Figure 13: Variogram model of the horizontal displacements, generated using the same method as Figure 12. The range appears to be approximately 900 m - 1000 m, with the final point measurement deviating from the trend. The silt is less defined in this plot. This is believed to be due to interference at the boundary choice.

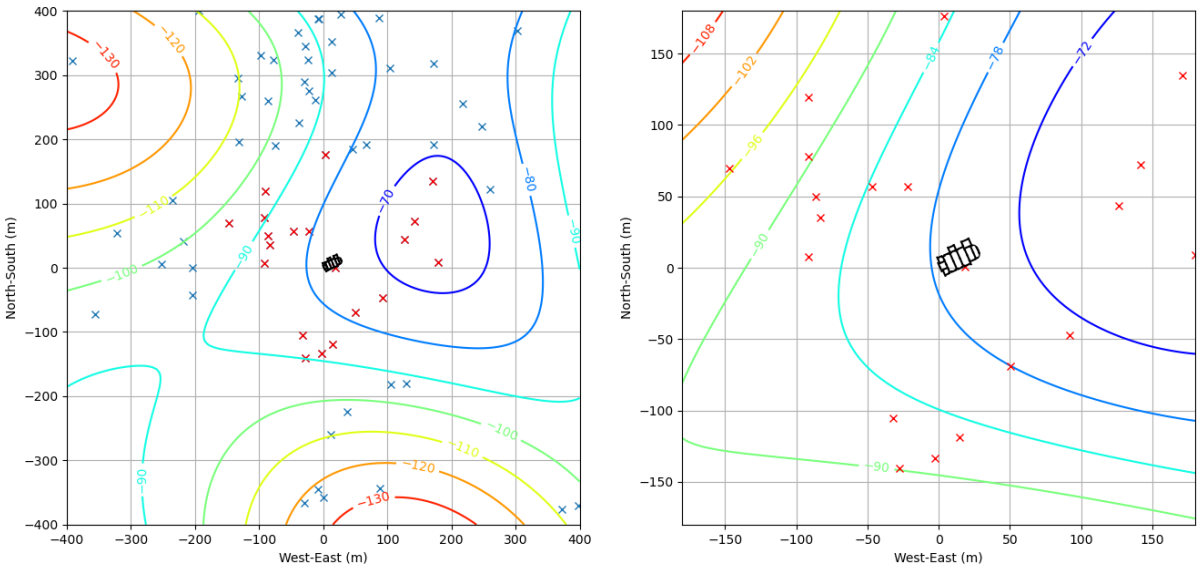

Figure 14: Interpolated cumulative vertical displacements from 2014-12-16 till 2017-03-23. The crosses indicate the points retrieved from the MT-InSAR analysis, of which the red ones are used in the local-scale model. The structure appears to be on a curving surface as the distance between the contour lines varies and the angles change.
(*A 3D visualisation of this figure can be seen in Figure 15.*)

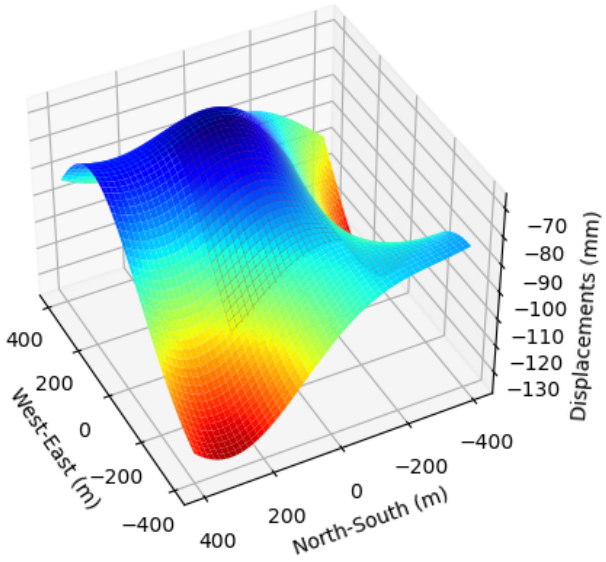

Figure 15: Alternative representation of Figure 14, interpolated cumulative vertical displacements on 2017-03-23 since 2014-12-16. With the internal raster representing the local-scale model and the origin $x = 0$ and $y = 0$, being the front entrance of the church.

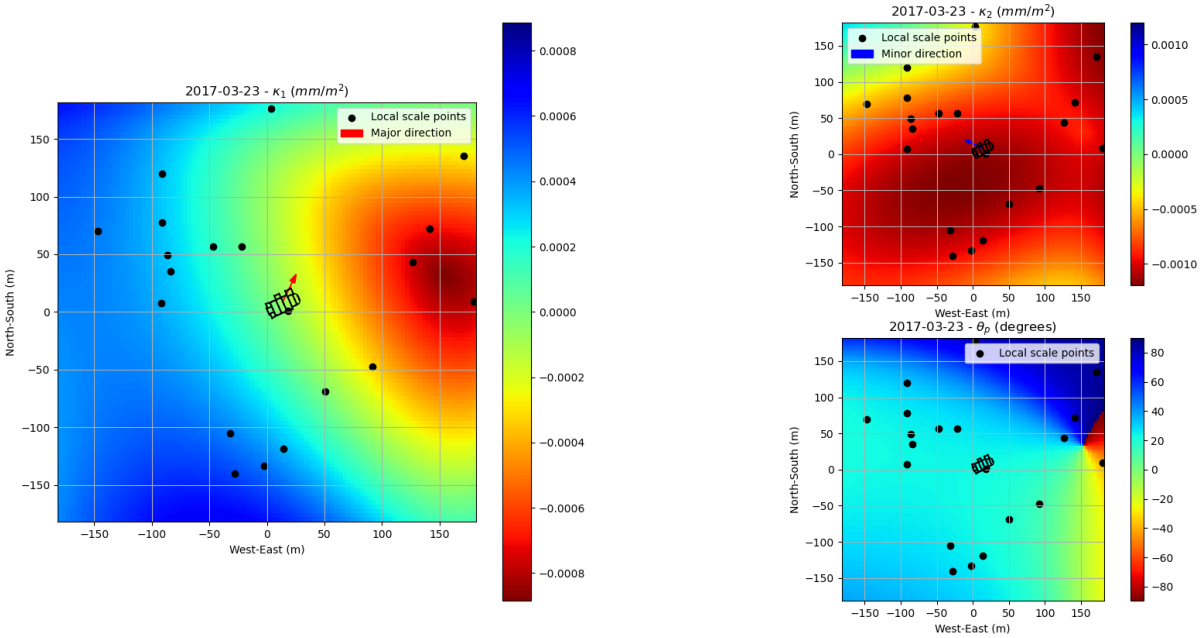

Figure 16: Interpolated cumulative vertical principle curvatures from 2014-12-16 till 2017-03-23. As confirmed in Figure 14, most curvature is along the North-West to South-East direction, corresponding with the second principle direction. In this plot, it is also apparent that the curvature isn't constant at the scale of the points included in the local-scale model.

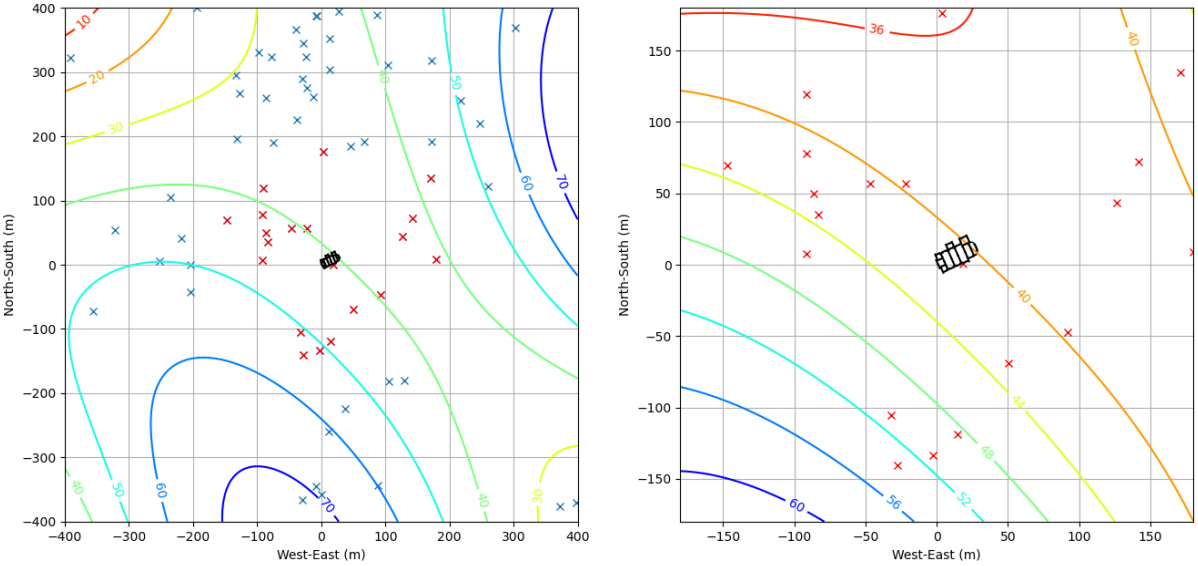

Figure 17: Interpolated cumulative horizontal displacements from 2014-12-16 till 2017-05-22. In both plots the crosses indicate the points obtained from the MT-InSAR analysis. The one on the right is the same result but plotted on the same scale as the local-scale model. In this case the church appears to be located on a mostly linear plane, since the contour lines are roughly parallel equidistant and straight near the church. There is a slight curvature along the length of the church which results in bending of the contour lines towards the South-East of the church.
(*A 3D visualisation of this figure can be seen in Figure 18.*)

timestamp with the greatest cumulative displacement gradient is plotted. The curvature is an order of magnitude less than that of the vertical displacements at the church, as shown in Figure 19.

3.2.2 Discussion

In the vertical deformations, there is a clear indication of curvature based on Figure 16. Therefore, it is useful to have a second or third order polynomial when performing least squares. Higher order polynomials allow for more freedom but can result in a wavy shape. In addition, the accuracy decreases as the number of unknown coefficients increases, as shown in Equation 3. The church is believed to be most influenced by either a settlement difference along the width, affecting the brickwork arches, or curvature along the longitudinal direction. The latter results in bending of the nave walls. The horizontal deformations assume the shape of a flat plane, as shown in Figure 17. To account for this, only a first order polynomial is strictly required. However, a second order polynomial, could be beneficial if the slope does change slightly. Regarding the structure, any horizontal difference would result in either shear, compressive or tensile behaviour in the structure's walls.

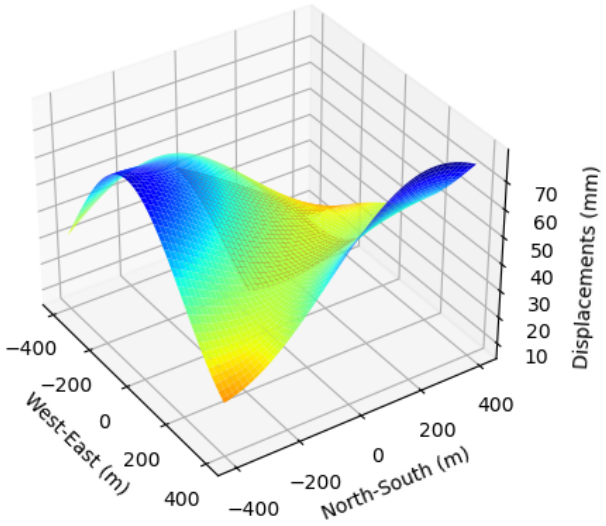

Figure 18: Alternative representation of Figure 17, interpolated cumulative horizontal displacements on 2017-05-22 since 2014-12-16. With the internal raster representing the local-scale model and the origin $x = 0$ and $y = 0$, being the front entrance of the church.

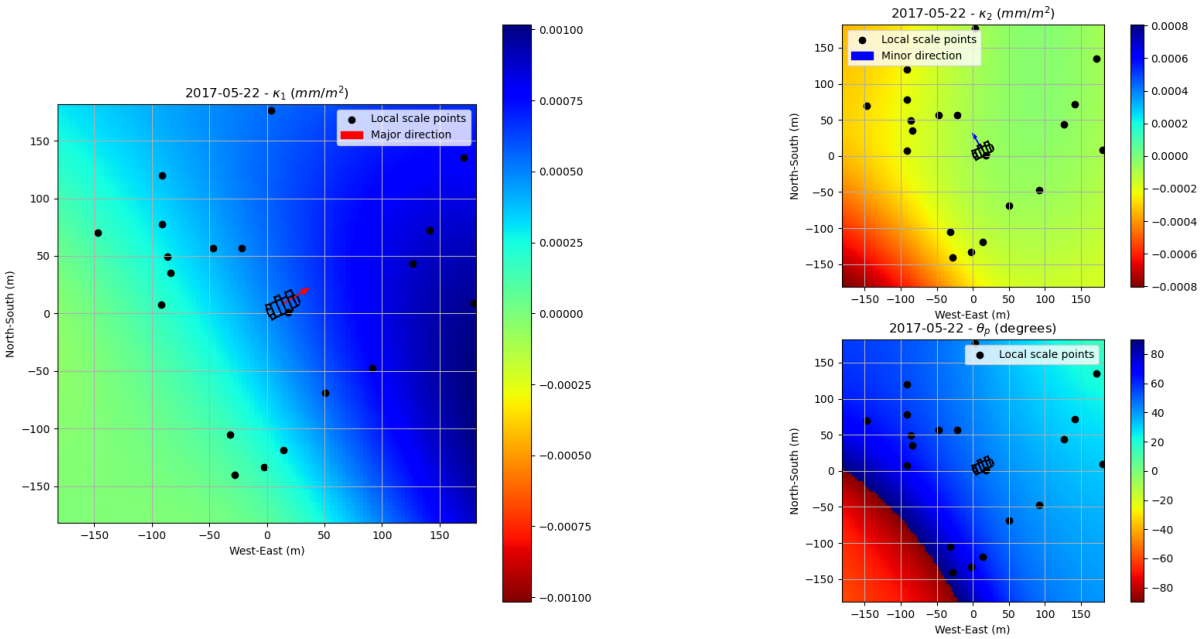

Figure 19: Interpolated cumulative horizontal principle curvatures from 2014-12-16 till 2017-05-22. The curvature's value is general low, resulting in less than 0.1 mm differential displacements over 30 m at the peak magnitude.

$$N_{coefficients} = \frac{(order + 2)(order + 1)}{2} \tag{3}$$

3.3 Local-scale model

The local-scale model uses the least squares method to obtain the best fit for a chosen polynomial function. Like the large-scale model, the fitting is performed for each set of cumulative displacements at a particular timestamp.

The approach is divided into three steps. The first step is to establish the polynomial order and the number of observations that have been included in the analysis. Next, the best fitting coefficients are determined for each timestamp individually. The last step is to apply a filter on the estimated coefficients as a function of time.

The polynomial order is primarily based on the discussion of the large-scale model in subsection 3.2.2. In addition, the points closest to the church, in this situation a single persistent scatter, has been excluded from the fitting process for testing and is used to evaluate the polynomial order and effect of the included region size. The polynomial order is decided best on the number of persistent scatters or observations for least squares, and the estimation error in the testing point. The size is then selected by minimising the estimation error of the same point.

After performing the least squares computation, the polynomial coefficients are filtered. This is done to reduce high-frequency deformation changes or potential noise, which are not expected to be present in this situation. To do this a Savitzky-Golay filter[6] has been applied.

3.3.1 Application and results

Only 1 persistent scatter point has been obtained from the MT-InSAR analysis at the church. The next closest point is appropriately 50 m further away. This scatter has been excluded to evaluate the variation of the estimation error when considering both the polynomial order and the number of persistent scatters. For the vertical displacements a third order polynomial (Equation 5) has been chosen, as it showed a lower estimation error, than fourth or second. The horizontal displacements showed no variation in error when including third order terms, in which case a second order polynomial (Equation 4) with fewer coefficients is more favourable. In addition, based on the estimation error, 21 persistent scatters have been included, which are situated in a square region with a width of 360 m. With more points, the error decreases until 21 have been included, after which increasing the region causes little variation on the horizontal deformations. The points and estimation error are shown in Figures 20 and 21.

[6] A low-degree polynomial fitting to successive sub-sets using linear least squares.

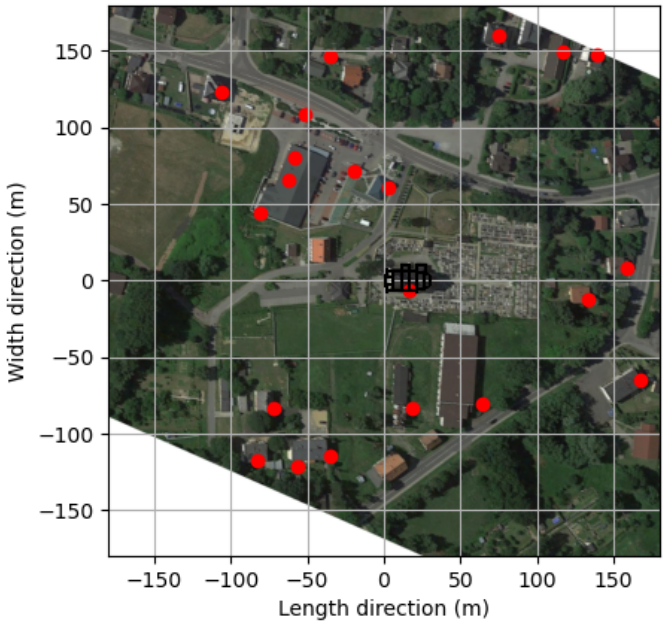

Figure 20: The 21 points included in the local model applying least squares. The points are all within a square region with a length of 360 m. All points appear to be located on better reflective surfaces with less scatter, which results in fewer points in the lower-right corner. The coordinate system is rotated to align with the structure and East is located at an angle of -24 degrees around the z-axis.

$$f_2(x, y) = c_{00} + c_{01}y + c_{02}y^2 + c_{10}x + c_{11}xy + c_{20}x^2 \tag{4}$$

$$f_3(x, y) = c_{00} + c_{01}y + c_{02}y^2 + c_{03}y^3 + c_{10}x + c_{11}xy + c_{12}xy^2 + c_{20}x^2 + c_{21}x^2y + c_{30}x^3 \tag{5}$$

Vertical displacements

The church, on average, settles approximately 12cm over the course of 6 years, shown in Figure 25. The majority of the settlements differences, are caused by linear terms in the polynomial of Equation 5, accounting for a difference of 16 mm of the 20 mm over six years. The most differential displacement is observed after 826 days, after which the displacements remain relatively constant, as shown in Figure 22. The church is on a settlement gradient from the front to the rear section, with a slight slope from left to right, as shown in Figure 23. Figures 23 and 24 show the principle curvature magnitudes and angle. The major principle curvature is relatively constant and is at an angle of 60° with the longitudinal direction. The absolute settlement difference due to curvature is low, with a displacement difference of approximately 1 mm to 2 mm, based on the magnitude.

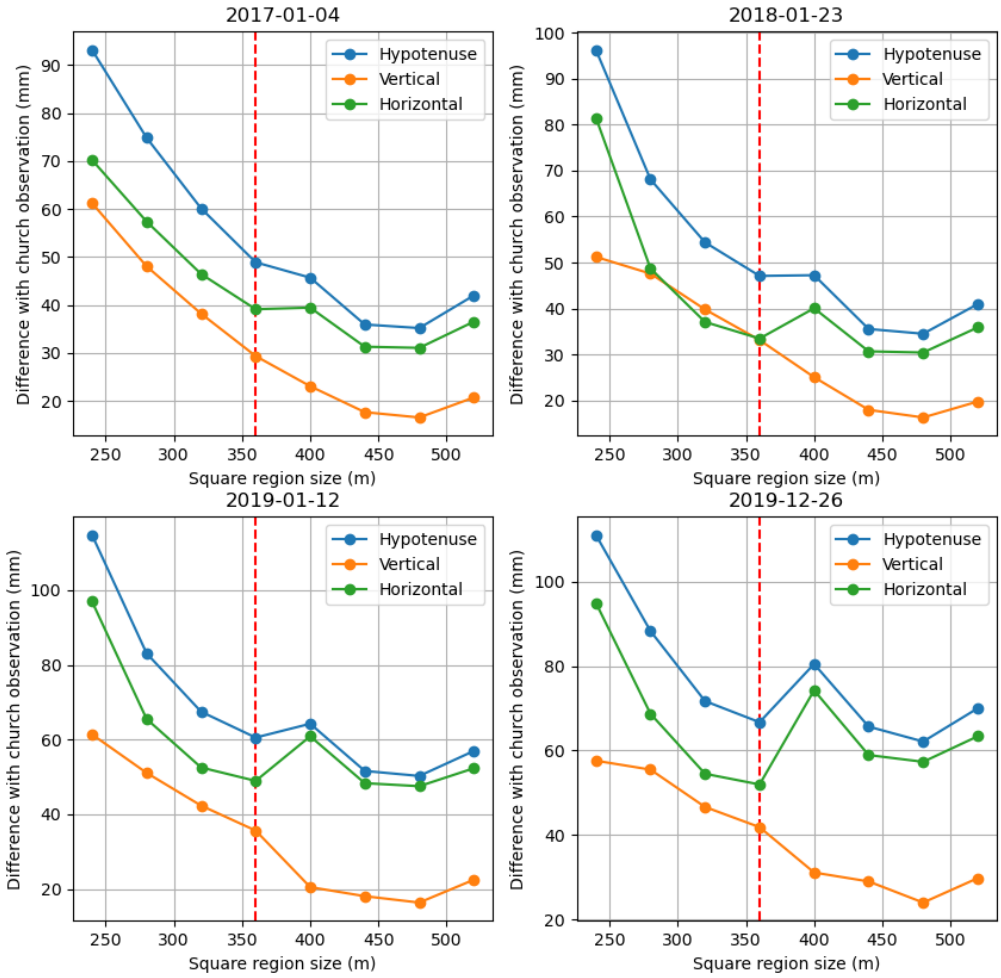

Figure 21: Cumulative displacement estimate error made at the point located on the church (Figure 20) as a function of the size of the square region within which points are included (x-axis). The point used to verify the estimate was not included when performing this analysis. The error is largest when only a few points are included, such as at 240 m with only 11 points. As more points are included, the estimation improves and reaches an optimal at appropriately 360 m (21 persistent scatters), indicated with the dashed red line. After this optimal, the error increases, and specifically for the horizontal displacements does not decrease.

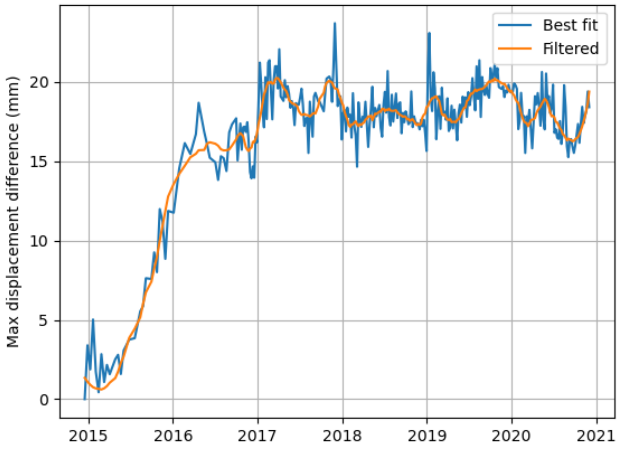

Figure 22: Extreme relative cumulative vertical displacement differences over the observation duration. The y-axis contains the maximum absolute difference between point pairs found in Figure 23. The filtered line is obtained after applying a Savitzky-Golay filter on each coefficient (Figure 25). This plot indicates when the vertical displacements are most critical and how the trend progresses over time. It can be seen that the slope is not constant, with the most difference occurring in the first years of observation.

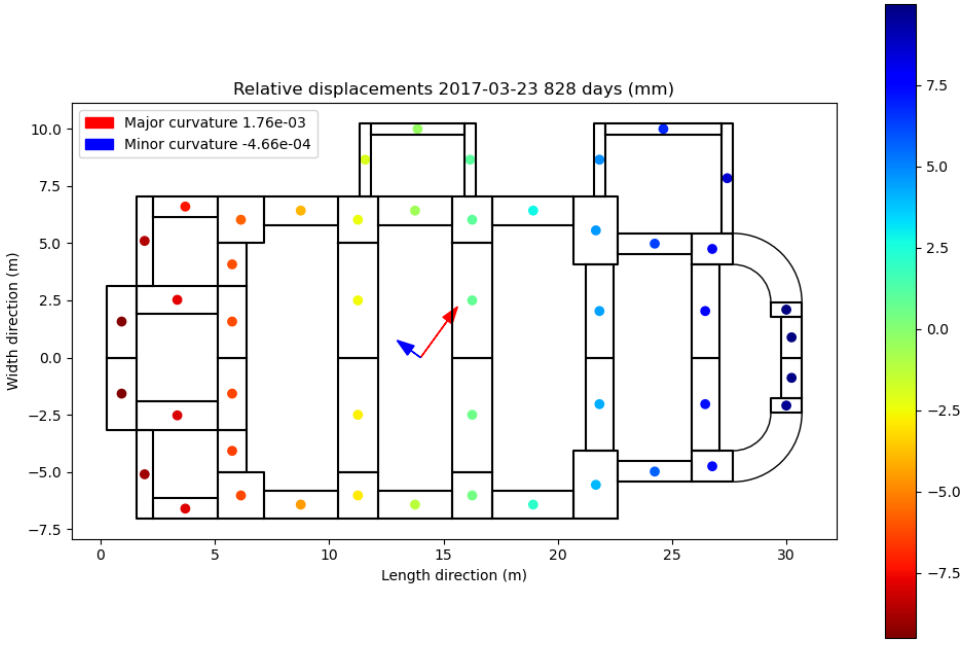

Figure 23: Relative filtered cumulative vertical displacement differences after 828 days of observation (critical timestamp). The figure indicates the estimated differences at various locations within the church and the magnitude and direction along which the principle curvatures act. Negative values indicate a downwards movement, implying in this plot that the tower section on the left settles more due to estimated mining settlements.

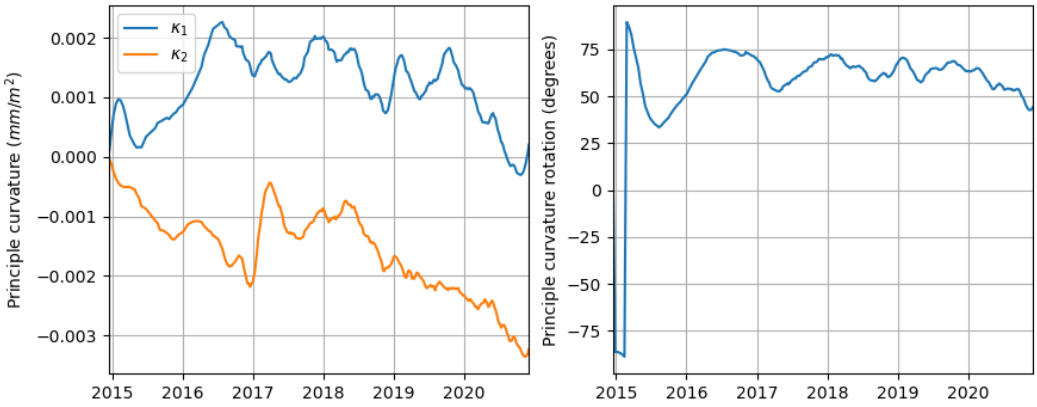

Figure 24: Curvature of the third order polynomial function (Equation 5) over time, taken at appropriately the centre of the church ($x = 14\ m$, $y = 0\ m$ in Figure 23). The plot on the left shows the principle curvatures κ_1 and κ_2. The plot on the right indicates the axis along which κ_1 is situated with respect to the x-axis of Figure 23. The figure shows that the curvature changes; initially, the curvature is appropriately along the width direction of the church, over time a combination of both length and width becomes critical. The magnitude suggests that curvature accounts for approximately 1 mm to 2 mm in differential displacement between the far ends of the church.

Horizontal displacements
Similar to the results of the large-scale model, virtually all displacements that occur are the result of the linear terms. The gradient is most pronounced along the x-axis, or longitudinal direction of the structure, as shown in Figure 26. The church tower is being pushed towards the rear of the church, with a difference of approximately 8 mm, shown in Figures 27 and 28.

3.4 Discussion

On the scale of the structure, the local-scale, Kriging would have been inappropriate. This is due to the low spatial density of the persistent scatters around the church. The variogram requires a much larger region to be reliable, and becomes inaccurate when considering interpolation differences at the church.

In general, the applicability of the approach with the interpolation methods, either the least squares or the Kriging, depends on the cause and effected scale of the deformations. Specific scenarios such as a local excavation or the boring of a tunnel, for instance, are likely incompatible with this approach. This is because of the low amount of persistent scatters covering the deformation, and the influence of the remaining PSs included on the interpolation. Kriging would be impossible due to the lack of a reliable variogram. Least squares would require a different model to account for local disturbances better. For the situation of mining deformations, both interpolation models are suitable. These

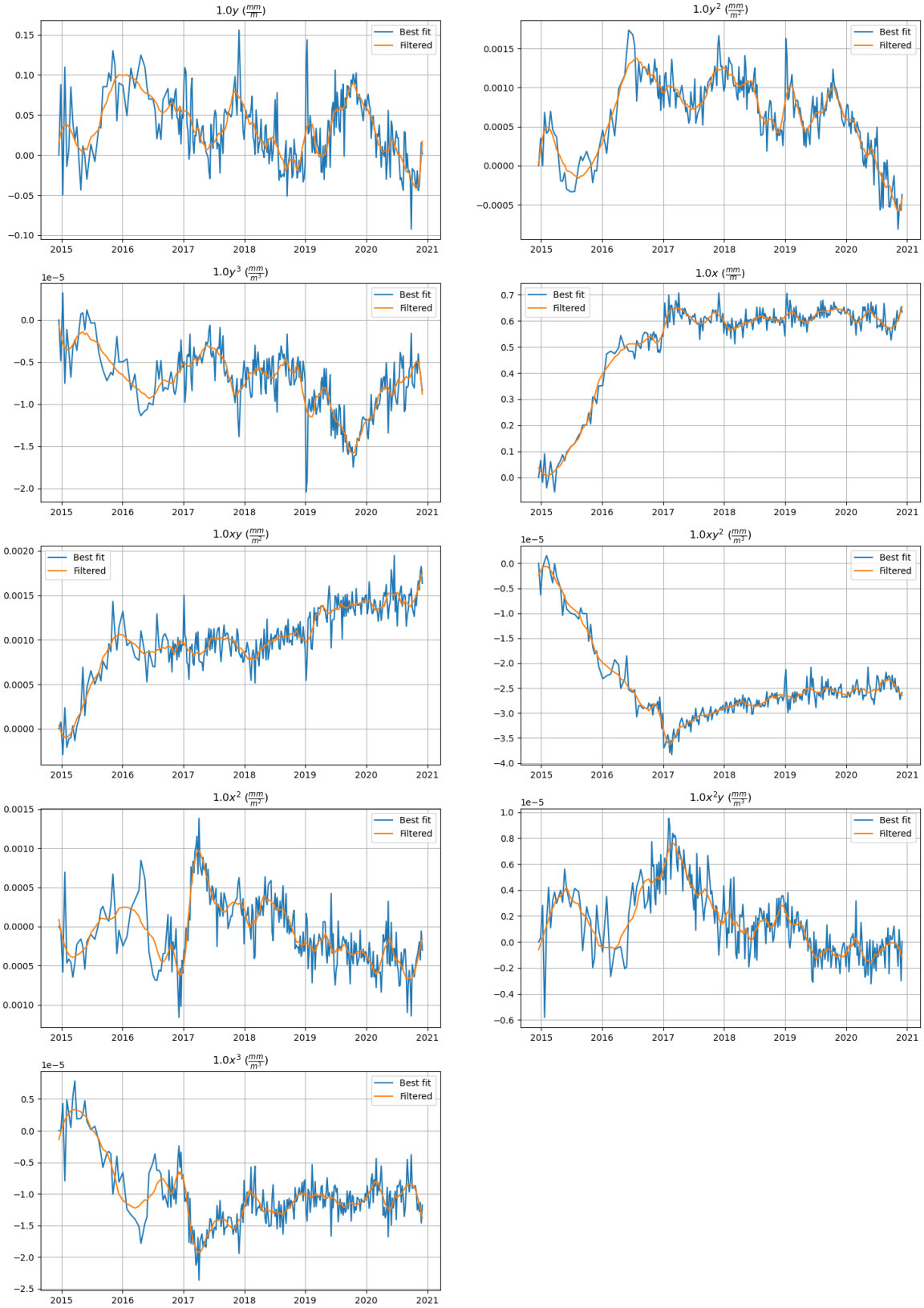

Figure 25: Coefficients of the least squares fit for the cumulative vertical displacements. Each plot has a title that indicates the relevant coefficient in Equation 5. A Savitzky-Golay filter has been applied to reduce the noise on each coefficient. From the plots, it is apparent that most of the displacements are either constant or linear.

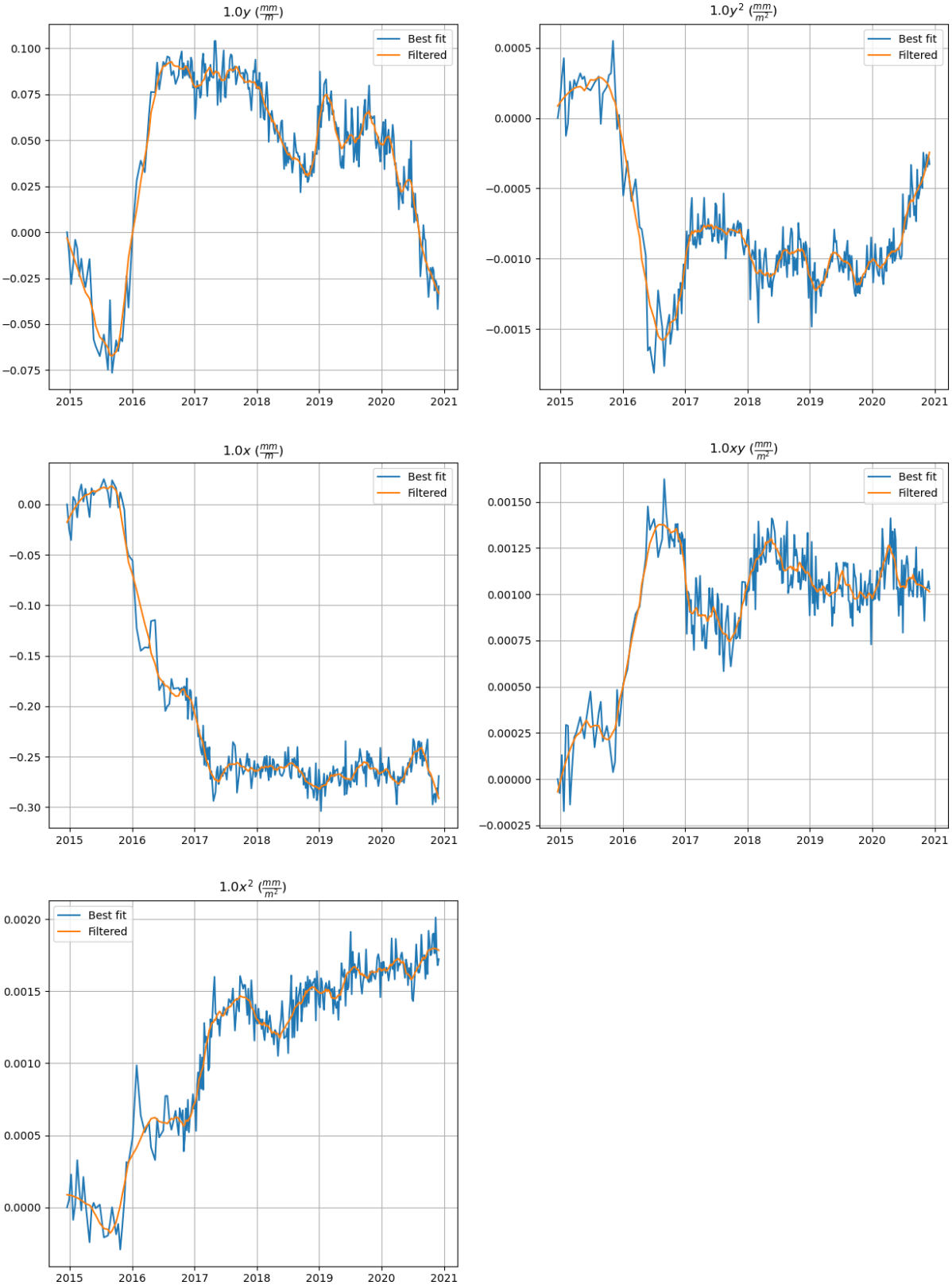

Figure 26: Coefficients of the least squares fit for the cumulative horizontal displacements. Each plot has a title that indicates the relevant coefficient in Equation 4. A Savitzky-Golay filter has been applied to reduce the noise on each coefficient. In the plots, it is apparent that most of the displacement is either constant or linear.

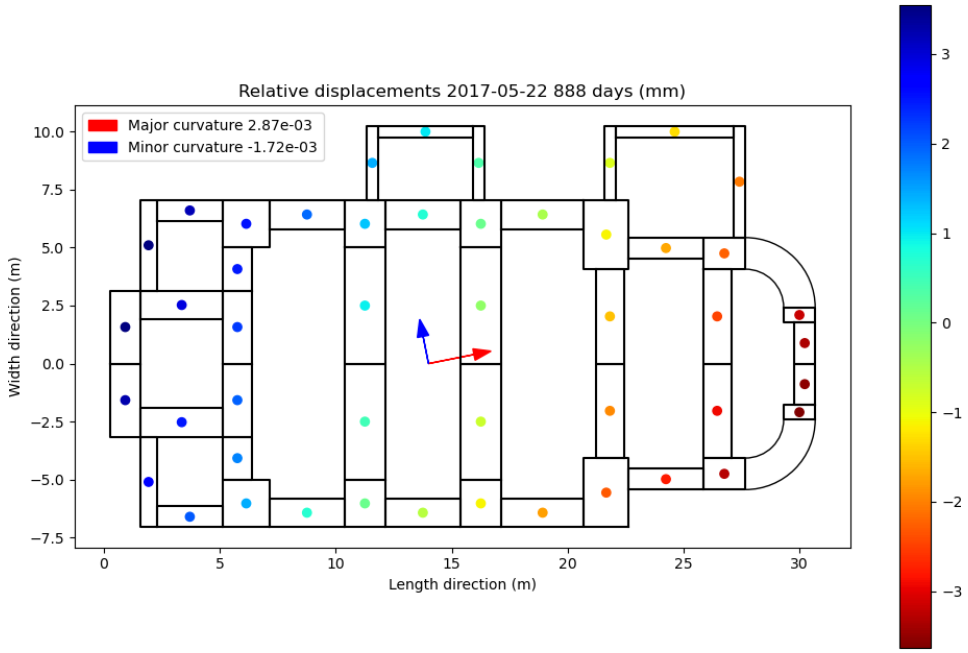

Figure 27: Relative filtered cumulative horizontal displacement differences after 888 days of observation (critical timestamp). The figure indicates the estimated differences at various locations within the church, as well as the magnitude and the direction along which the principle curvatures are. Positive values indicate an East-wards movement at a 24 degree angle with the x-axis. The values in the plot indicate a compressive load on the structure along the length and slight shearing along the width of the church.

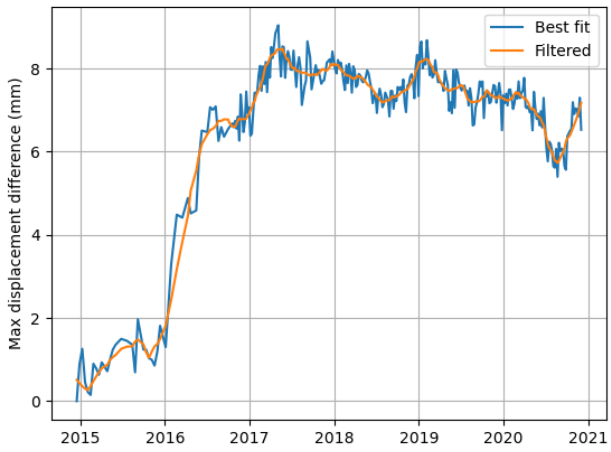

Figure 28: Extreme relative cumulative horizontal displacement differences over the observation duration. The y-axis contains the maximum absolute difference between point pairs found in Figure 27. The filtered line is obtained after applying a Savitzky-Golay filter on each coefficient (Figure 26). This plot indicates when the horizontal displacements are most critical and how the trend is progressing over time. The displacements build up approximately linear for the first two years and remain almost constant for the remainder of the time. The critical timestamp appears to be late May 2017.

deformations impact a large enough region for there to be a low spatial variance between the persistent scatters. In addition, the deformations are unlikely to only locally affect a single building due to the depth of the coal mine. The depth is over 700 m below the soil surface, which should distribute over the soil layers as it approaches the surface. Other applicable situations could be consolidation of the soil due to changes in the groundwater level or large landslides.

There are limitations both with regards to performing an MT-InSAR analysis and LSQ. From the InSAR perspective, it is only possible to observe displacements along the line-of-sight. This ultimately provides us with a projection of displacements along the vertical and West-East direction, with the horizontal movement parallel to the North-South line being unknown. When horizontal displacements are expected to be present and the direction isn't known, as is the case here, the observation method falls short. In addition, when event local disturbances occur in the region over which the LSQ model is applied, they will be partially ignored and result in estimation errors elsewhere. This is due to the assumption of the polynomial shape, which is continuous and depending on the polynomial order, unable to change for a sub-region.

4 Structural model

The next part of the framework is to obtain a structural model. In this case, a finite element model using 3D nonlinear solid elements is analysed using DIANA FEA (software). For the church, certain simplifications have been made due to limited information and the influence of certain components.

A nonlinear FEM has multiple advantages. It can model arbitrary objects with nonlinear material behaviour, structural instability and incorporate nonlinear soil-structure interaction. For the church, only the masonry is modelled with nonlinear behaviour. This allows one to account for the crack propagation during the time history of the applied load, which in a strictly linear analysis would be impossible. The soil-structure interaction is modelled using linear elastic properties without the occurrence of tension in the vertical direction[7]. Furthermore, another advantage of a finite element analysis using solid elements is that the model's accuracy depends on the error propagation of the input, and the size of the elements.

This section starts by providing a background of the church and all information used to establish the model. The following subsections then discuss how the structural model has been set up, the response to the estimated self-weight, and a comparison with a linear elastic model and shell elements. In the model setup, the input geometry, chosen materials properties and method of modelling the soil interaction are mentioned. The response to self-weight discusses how the structure deals with the load to gain insight into important regions and partially validate the model setup. In the final subsection, the same model has been constructed by using shell elements, and a comparison has been made with the use of solid elements.

4.1 Background information

This subsection includes information of recent renovation work, a general description of the church and a few drawings and images, presented in Figures 29, 30 and 31. Dominika Malinowska has provided most information relating to the church.

The church was built in the Baroque and Classicist style. Since 1996, the structure has been included in the Polish Registry of Objects of Cultural Heritage for its artistic and historical importance. The largest section of the church is a long open nave, as shown in Figure 29. The roof and tower are supported by wide vertical masonry brick walls and arches. The main building is 31 m long, 14 m wide, and the roof ridge is 19 m above the floor level, with the tower reaching a height of 33 m. It has a timber roof structure that is relatively light compared to the total weight of the church and consists of battens on purlins supported by trusses above the arches. The church also contains two annexes of approximately 4 m in height.

[7]No tension in the vertical soil-structure interaction, is asserted after running the analysis and verifying that the interface elements do not exhibit tension. For illustration Figure 41, shows the reaction forces below the structure.

(a) Facing front-right view

(b) Facing towards the front entrance

(c) Facing the rear of the church

Figure 29: Closer view at the arches and placement of the choir platform.

The earliest known renovation was around 1990, during which steel ties were added to reinforce internal brickwork arches, upholding the ceiling, shown in Figures 29 and 30. Later renovations, in 2014 and late 2018, focused on fixing non-structural aspects. Some of the recent renovations have been founded by the mining cooperation.

During the late renovations the most noteworthy changes are the placement of local anchoring and the repair of cracks. These cracks occurred at door arches and along the longitudinal walls at window openings. The windows specifically have had replacements of cracked inserts. In addition to this, the floor has received reinforcement by adding of reinforced bands. Fortunately, given the importance of the structure, nothing was found that would warrant significant concern to the integrity of the building.

4.2 Geometry

The church shown in Figures 32 and 33 consists of a few different compartments separated by solid brickwork walls. In Figure 33, the main entrance is on the far right, with small compartments on either side and the tower above it. Behind the entrance is the main volume or nave of the church. Along the left elevation are two small annexes, as seen in Figure 37. All the main walls extend to a height of about 11 m above the floor level. The walls of the annexes are much lower with their gutter-level being 3.25 m from the floor level, with gables up to the underside of their roofs. The position of the doors/openings are shown in Figure 33. The windows are visible in Figure 32.

The church is founded on mass brickwork strip-footings, which are approximately $40cm$ wider than the walls located above it and $80cm$ deep. The church's timber roof structure and brickwork ceiling span and transfer their weights and loads to the main brickwork structure below. However, they hardly contribute to the integrity of the main structure with respect to the deformation loads at the foundation level. Hence their components have not been detailed in the model, but the self-weight has been added, further elaborated in Section 4.3. The structure as inputted into the finite element program is shown in Figures 35 and 37. Compared to the original drawing, curved corners have been straightened to simplify the input and because, in most cases, it is believed to contribute solely for decorative purposes.

The church has steel ties along the arches, which are believed to be UNP240 members, visible in Figures 34 and 36. These members were added around the 1980s, approximately 180 years after the initial construction. In addition to these ties, reinforcement has been added along the church's perimeter. This consists of mainly a single round 28 mm steel reinforcement bar with exception of the rear curved wall for which UNP100 profile has been added. The perimeter reinforcement has been ignored as it is believed only have a limited local effect. In addition, little information could be retrieved on the connections relating to the UNP profile.

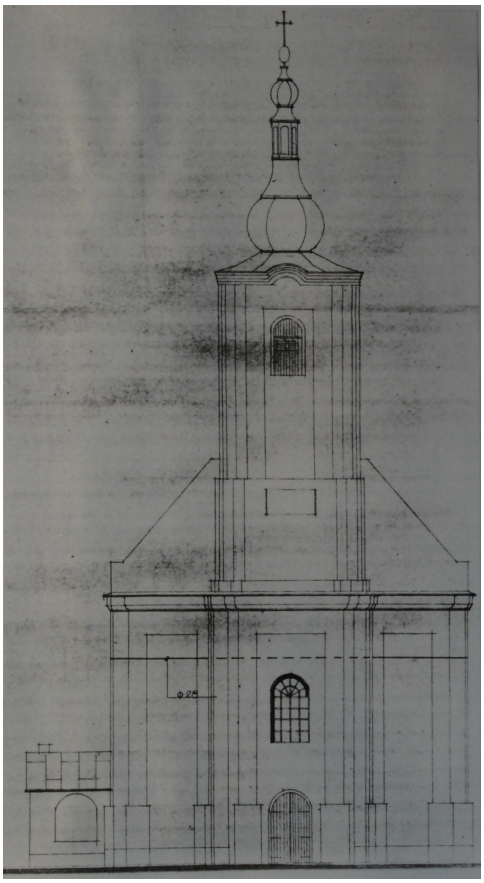

(a) Front facing view

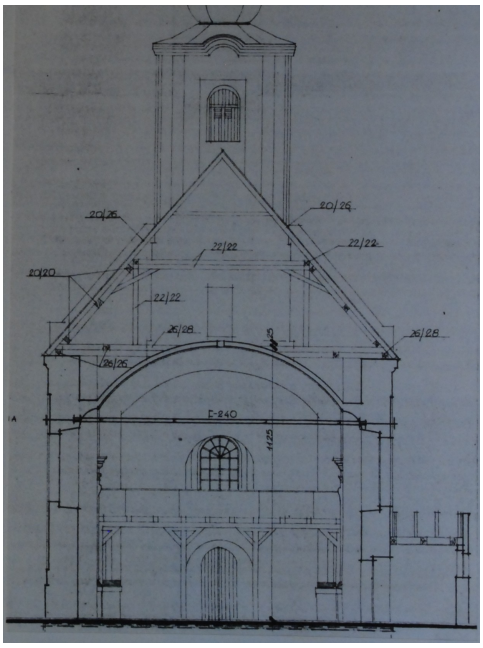

(b) Internal cross-section facing the front

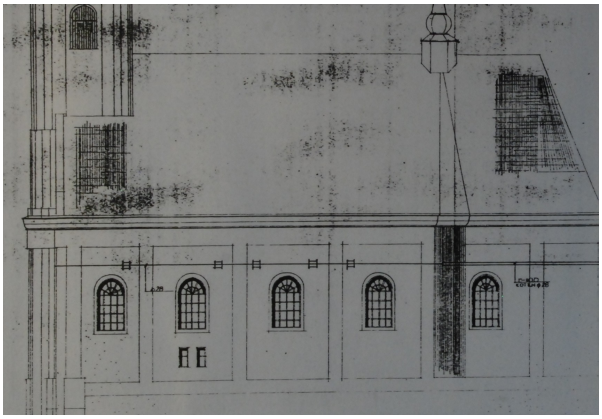

(c) Right side view

Figure 30: Vertical drawings obtained on the church.

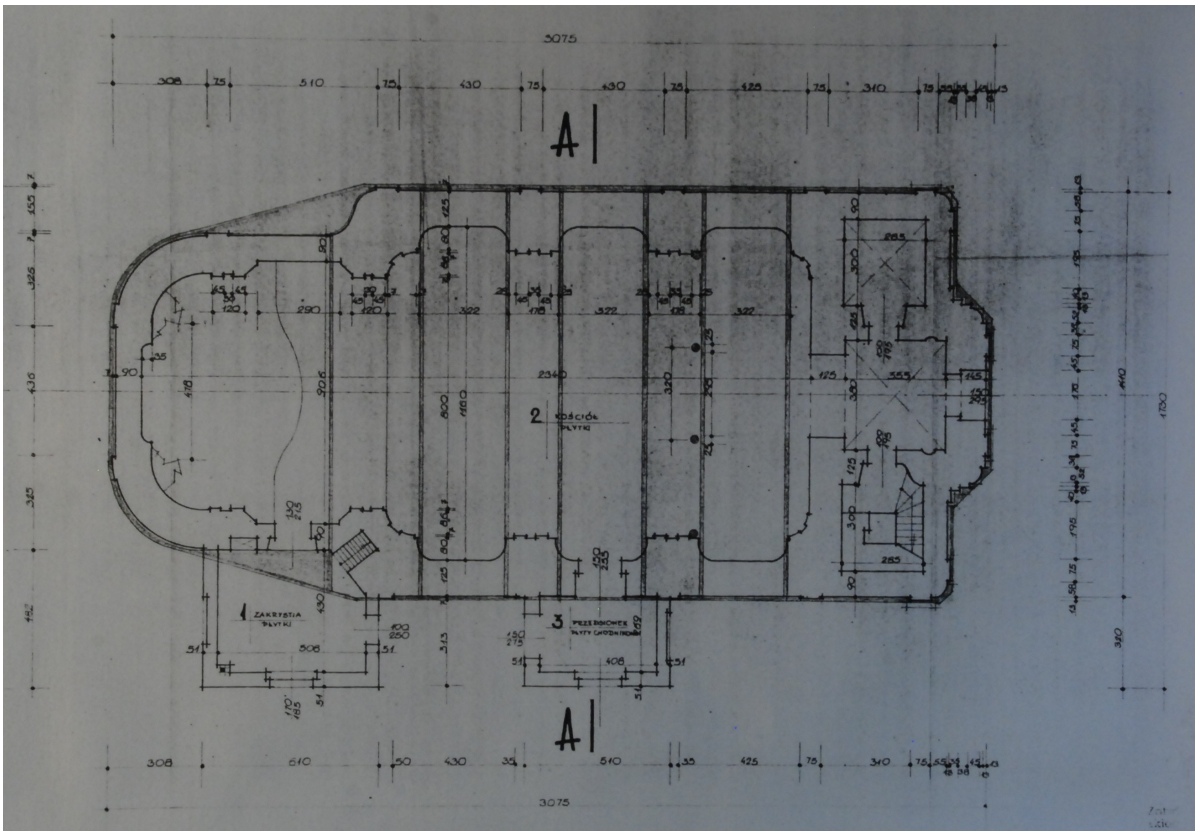

Figure 31: Horizontal cross-section from which most dimensions relating to the structure can be retrieved.

Figure 32: Outside view towards the front right of the church. The tower, windows and exterior decoration elements are shown in this image.

All significant openings have been added to the model, except the narrow stairway up to the pulpit, of which little is known other than its location within a large pillar (Figure 33, top-right of the left annex). Raking and sloping sides of the window openings have been simplified by approximating the size of the opening at their volumetric centre. Small curves and decorative parts of the pillars have been removed.

4.3 Accounting for the ceiling and roofing

Only the masonry walls, arches and foundation have been included in the finite element model. The roof and ceiling have been excluded from the model. However, they do impose a load on the church, specifically on the brickwork arches. Therefore their weight has been added using distributed loads.

4.3.1 Additional load at the tower section

The turret on the top of the tower roof, as shown in Figure 32, is most likely constructed with a frame and zinc sheets. The weight consists of three parts. The first is the sheet estimated at 0.15 kN/m^2. The second is the bordering holding the sheets estimated at 0.20 kN/m^2. And finally, the frame itself is estimated to be 0.25 kN/m^2. Together amounting to 0.60 kN/m^2 acting on the area of the tower roof.

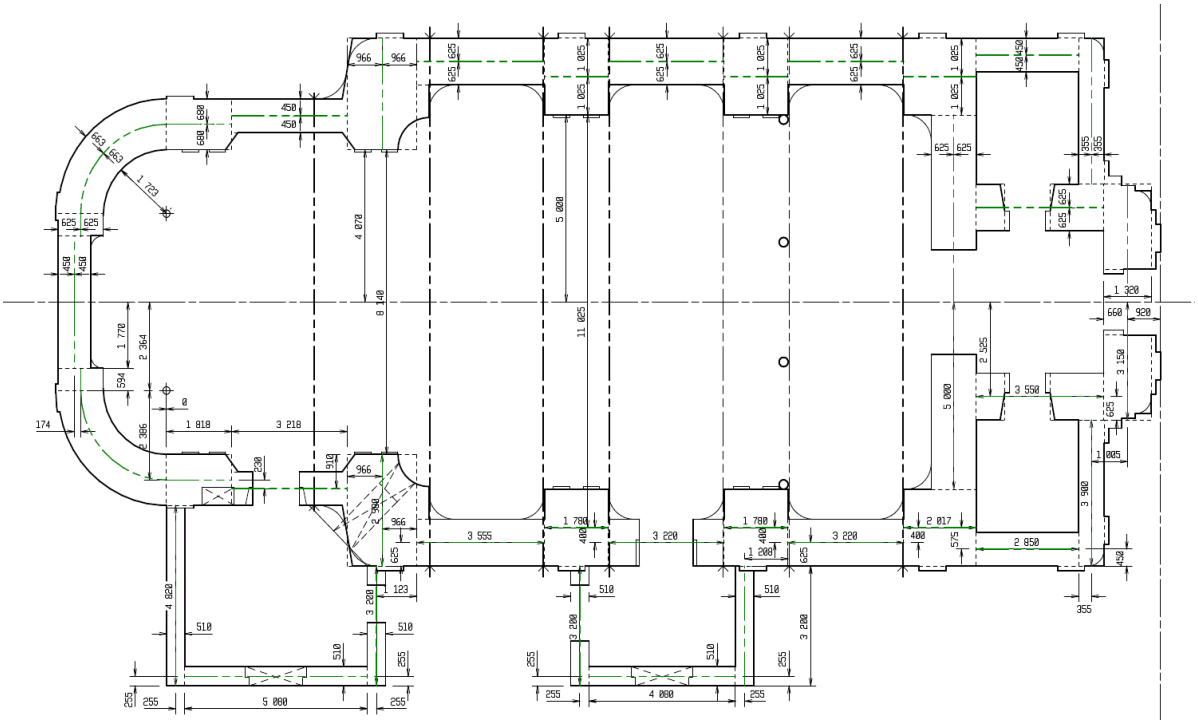

Figure 33: Cross-section of the church at the floor level. The main entrance is on the far right and the side annexes are in the bottom left and bottom centre. Secondary entrances are located on the side annexes. A choir platform is located directly beyond the main inner entrance (Figure 34), with the columns supporting the deck indicated on the drawing.

Figure 34: Inside view towards the front entrance and organ.

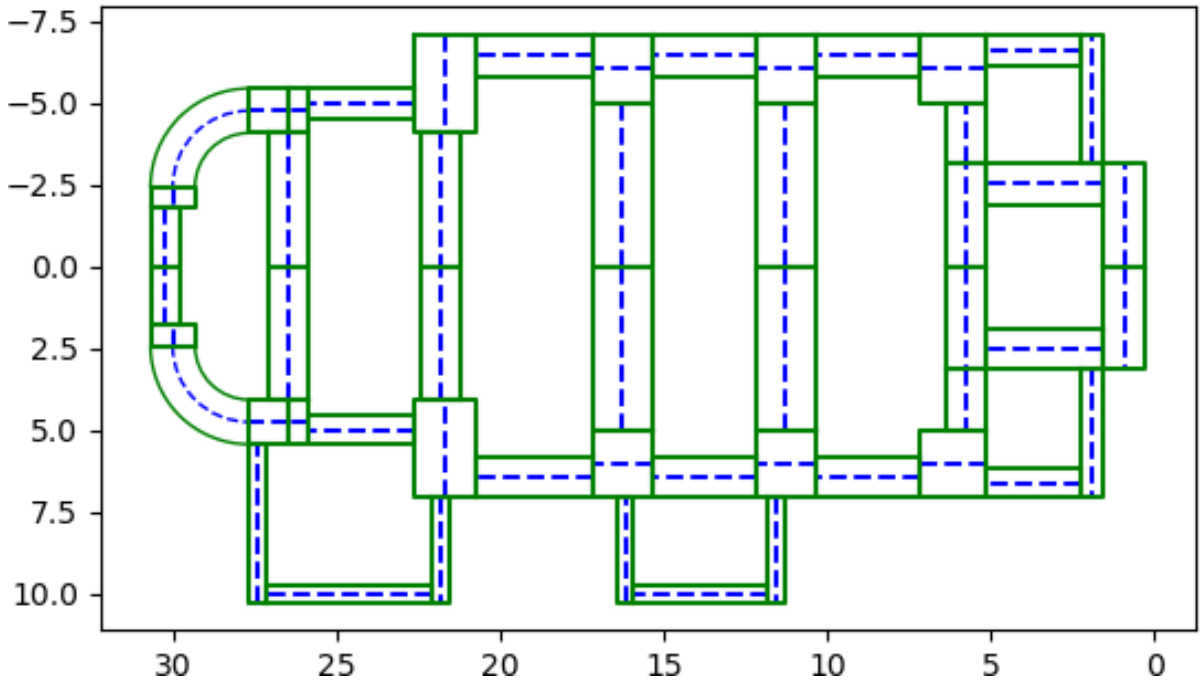

Figure 35: Cross-section of the church as inputted into the structural model. Compared to Figure 33, multiple curved corners have been replaced with rectangular corners, and the openings/windows are no longer visible. In this figure, brickwork arches spanning across the nave are indicated, also visible in Figure 34. The green lines indicate the outline of the structure and the blocks created in the solid finite element model. The blue dashed lines show the centre lines of the green blocks.

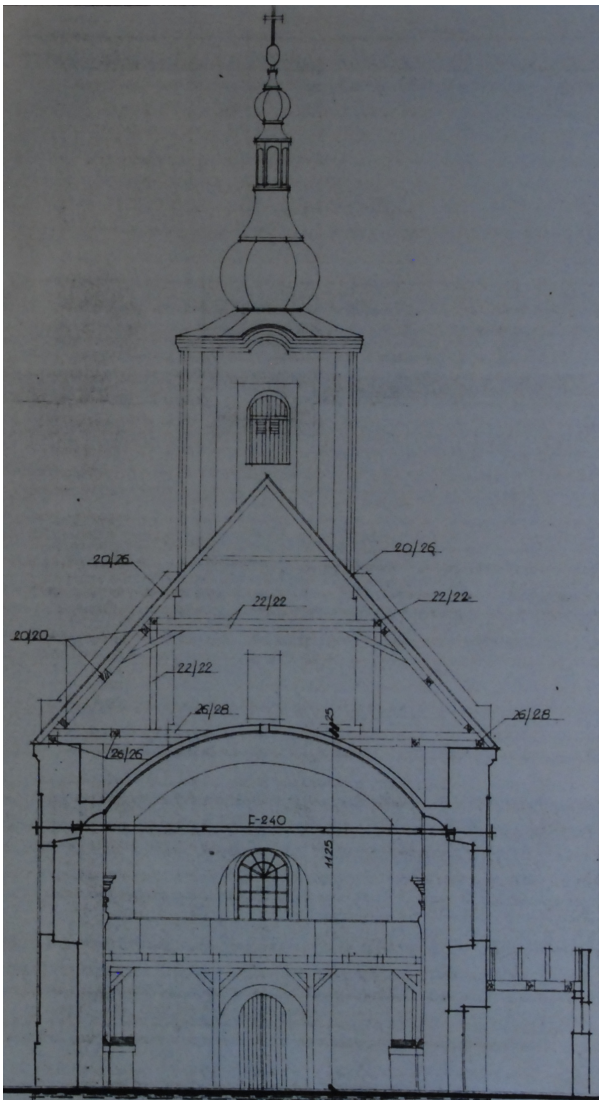

Figure 36: Vertical cross-section of the church at the first centre annex (Figure 33).

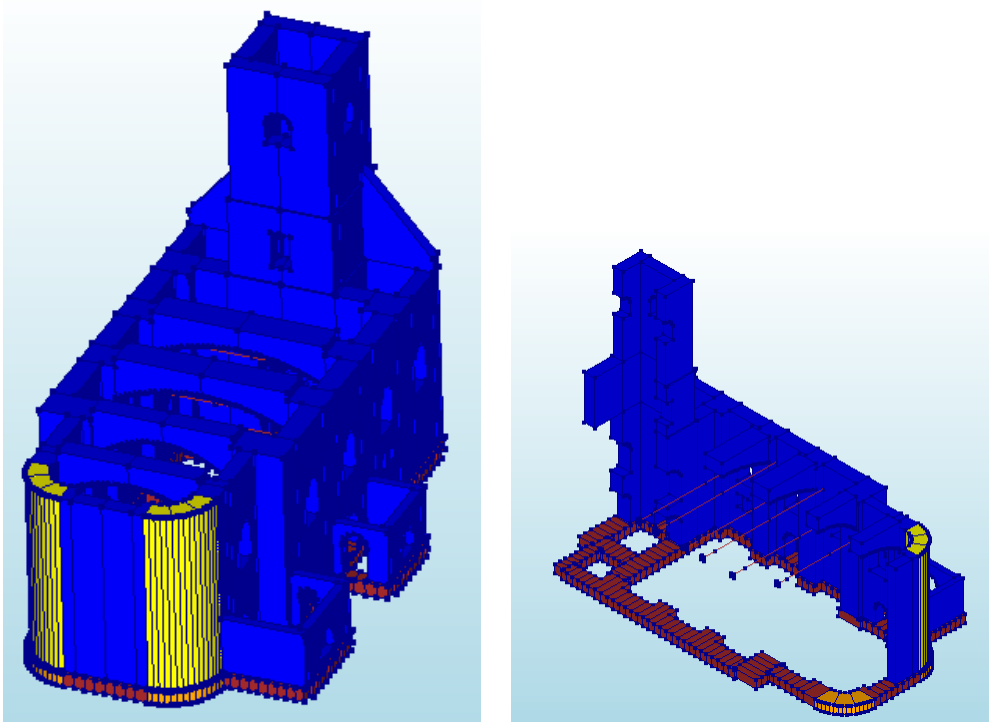

(a) Full model (b) Partial model

Figure 37: 3D model of the geometry. Blue/yellow represents masonry walls, red/orange blocks are the foundation walls, and red lines represent steel ties (visible at arches).

In the tower, there are five bells, with masses equal to 100 kg, 150 kg, 300 kg, 800 kg and 900 kg.

4.3.2 Additional load due to the general roof and ceiling

The roof is at a slope of approximately 50°, is covered using wooden shingles and is supported by a series of trusses (Figure 36). These are estimated to weigh on the sloped area 0.25 kN/m^2 and 0.30 kN/m^2, respectively. Based on the slope, the roof weighs approximately 0.86 kN/m^2 on a horizontal surface. The curved ceiling is comprised of brickwork with plaster, of which the brickwork is assumed to be 250 mm thick. The curvature is low, with the exception at the edges. The ceiling is estimated to be a constant arc, with a sagitta of 600 mm over the span of 4300 mm. This results in a length factor of about 1.09 per unit length horizontally. The final estimate of the ceiling weight on a horizontal surface is 4.9 kN/m^2, significantly more than the roof.

Based on the cross-section in Figure 36, the ceiling and roof appear to be bearing on the arches and walls. A part of the load close to the walls is assumed to be transferred to the wall segment (800 mm). The remainder is assumed to be bearing on the arches, especially the ceiling. An example of the final loads is shown for a brickwork density of 1900 kg/m^3 in Table 1.

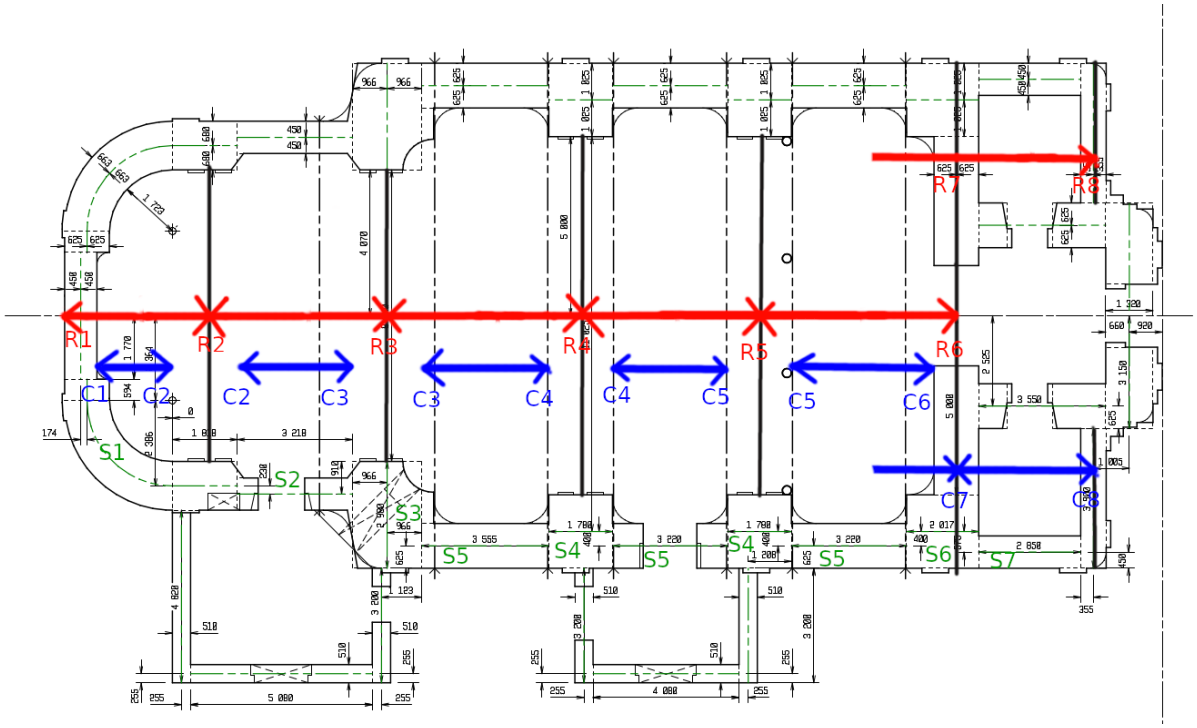

Figure 38: Roof and ceiling load scheme. R1 through R8 are considered as roof load paths. C1 through C8 are considered for the ceiling. S1 through S7 are direct loads bearing on the walls, both roof and ceiling load.

Index	**Roof (R, m)**	**Ceiling (C, m)**	**Load R+C (kN/m)**	**Load S (kN/m)**
i	r	c	$0.86r + 4.9c$	
1	2.3	1.1	7.4	5.8
2	4.1	2.9	17.7	5.8
3	5.2	3.9	23.6	1.7
4	5.3	4.0	24.1	1.8
5	5.0	3.7	22.6	5.8
6	2.4	1.8	10.8	1.8
7	4.9	3.6	22.1	5.8
8	1.9	1.7	9.9	

Table 1: Table of loads according to plan Figure 38, based on a brickwork density of 1900 kg/m^3. Note that S3,S4 and S6 have no ceiling load but have direct roof-loads.

4.4 Material properties

There are two main methods used when modelling cracks. The first is discrete crack modelling, in which bricks/blocks and joints are distinguished. The main benefit to this method, especially if the blocks approach the size of the bricks, is that it allows for accurate modelling of the crack patterns. The second method is a continuum element model. In this case, the cracks are smeared over a certain height within an element (crack bandwidth). The advantage is that less elements and often fewer material properties are required. Regarding the cracking, this method would allow cracks to develop in places that may vary slightly from the places in the actual structure due to the bricks and joint orientation. As a result, given the same tensile strength as a discrete model, cracks tend to occur sooner. On a large scale, however, with a correct choice of parameters, a continuum model accurately predicts crack locations and approximates their orientation.

Due to a lack of information and the scale of the model, it has been opted to use a continuum model instead of a discrete model when modelling cracks. Regarding the material properties, the decision has been made to only model tensile failure and not account for any crushing effects. This choice has been made since crushing is not believed to be a concern, and it reduces the number of uncertain parameters. A summary of the material properties is provided in Table 2.

To model the tensile behaviour, a rotating crack model with both linear and exponential softening is evaluated (Figure 39). These stress-strain relations require a few additional parameters. By specifying a rotating crack model, the crack orientation follows the principle tensile stress and no shear stiffness needs to be specified. Another advantage of specifying rotating cracks, particularly if the elements cross multiple physical bricks, is that the rotation can change with the propagation direction. The crack bandwidth is set to use Rots, which is based on the element size.

Mass density	1800 - 2000 kg/m^3 (default 1900)	
Young's modulus	1000 - 6000 N/mm^2 (default 3000)	[Drougkas et al., 2020a]
Poisson's ratio	0.2	
Crack orientation	Rotating	
Tensile curve	Linear/exponential crack energy	
Tensile strength	0.05 - 0.2 N/mm^2 (default 0.10)	[Drougkas et al., 2020a]
Fracture energy (mode I)	1 - 50 N/mm (default 5)	[Drougkas et al., 2020a]
Crack bandwidth specification	Rots	
Compressive curve	Linear elastic	

Table 2: Masonry material properties used in the structural model.

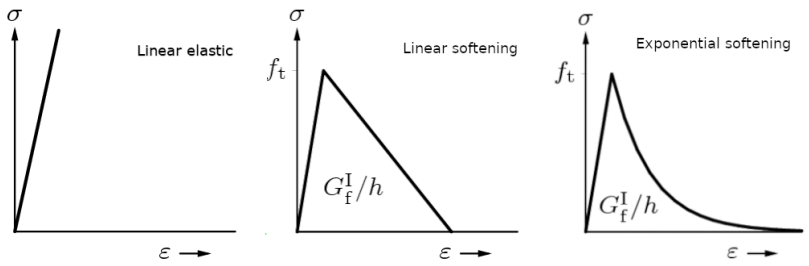

Figure 39: Tensile stress-strain curves.

4.5 Soil interaction and deformation input

A layer of interface elements is present between the foundation walls and the application of the deformations obtained from the local-scale deformation model (section 3.3). These interface elements have been added to account for some soil-structure interaction. The vertical stiffness is determined by dividing a typical Young's Modulus of the soil by an arbitrary length. The horizontal stiffness has been set to half the vertical stiffness. The advantage of adding this interface is that the structure can deviate from the inputs, allowing the load to be spread in a more realistic manner. The other benefit is that there is some margin for differential settlements due to the self-weight of the structure, specifically the tower section.

The elastic modulus has been obtained from Table 3 with the description of Figure 40. The result is that the modulus is taken between $24 N/mm^2$ and $190 N/mm^2$, corresponding with "sandy clay" and "dense sand and gravel" per Table 3. The arbitrary height range has been chosen from 1 m till 5 m. The resulting stiffness obtained ranges between $4.8 MN/m^3$ and $190 MN/m^3$, which is a broad range. The default is chosen at the midpoint, resulting in $95 MN/m^3$ for the vertical stiffness and $47.5 MN/m^3$ in the horizontal directions.

Soil	E (N/mm^2)	E (tsf)
Very soft clay	0.5 - 4.8	5 - 50
Soft clay	4.8 - 19.2	50 - 200
Medium clay	19.2 - 47.9	200 - 500
Stiff clay, silty clay	47.9 - 95.8	500 - 1000
Sandy clay	23.9 - 191.5	250 - 2000
Clay shale	95.8 - 191.5	1000 - 2000
Loose sand	9.6 - 23.9	100 - 250
Dense sand	23.9 - 95.8	250 - 1000
Dense sand and gravel	95.8 - 191.5	1000 - 2000
Silty sand	23.9 - 191.5	250 - 2000

Table 3: Typical Elastic Moduli [EM 1110-1-1904, 1904].

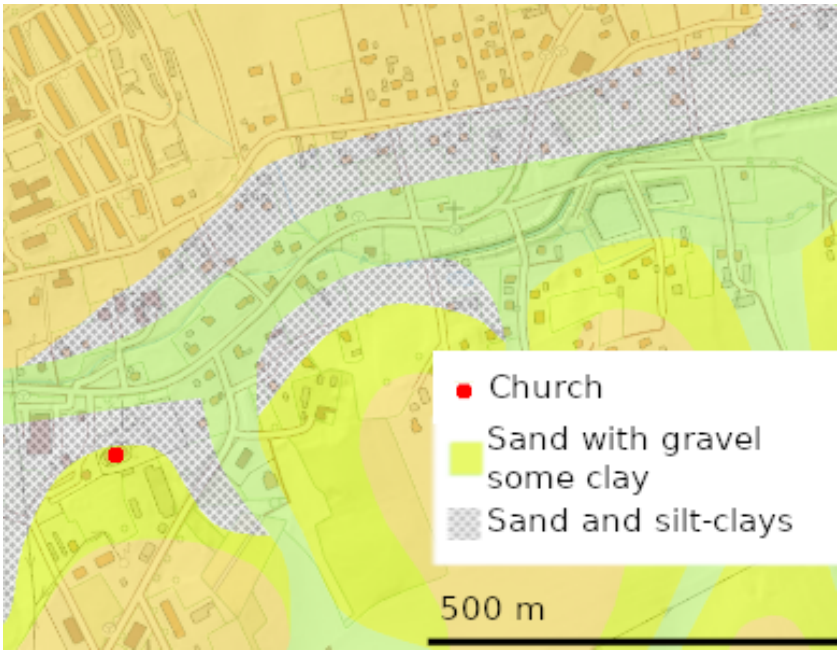

Figure 40: Soil type near the church [Institute, 2020].

4.6 Response to self-weight

In this subsection, the solid element model previously discussed has been evaluated using solely the self-weight and the default material and soil properties summarised in Table 4. The objective is to gain insight into the situation before adding the deformations computed in Subsection 3.3. Specifically the deformations, stresses and major principle crack width have been evaluated.

4.6.1 Horizontal and vertical deformations

The vertical deformations of the church are shown in Figure 42. The front/tower section of the church is the heaviest, showing the most settlement and the annexes with a limited wall weight deforming the least. The largest vertical deformations are observed

Property	Unit	Current	Minimum	Maximum	Default
E (masonry)	GPa	3	1	6	3
Tensile strength	MPa	0.1	0.05	1	0.1
Fracture energy	N/mm	5	1	50	5
Masonry density	kg/m^3	1900	1800	2000	1900
Vertical interface stiffness	MN/m^3	95	5	190	95
Horizontal interface stiffness	MN/m^3	47.5	2.5	95	47.5

Table 4: Variable properties used in the evaluation of the response to the self-weight. The remaining constant material properties are provided in Table 2.

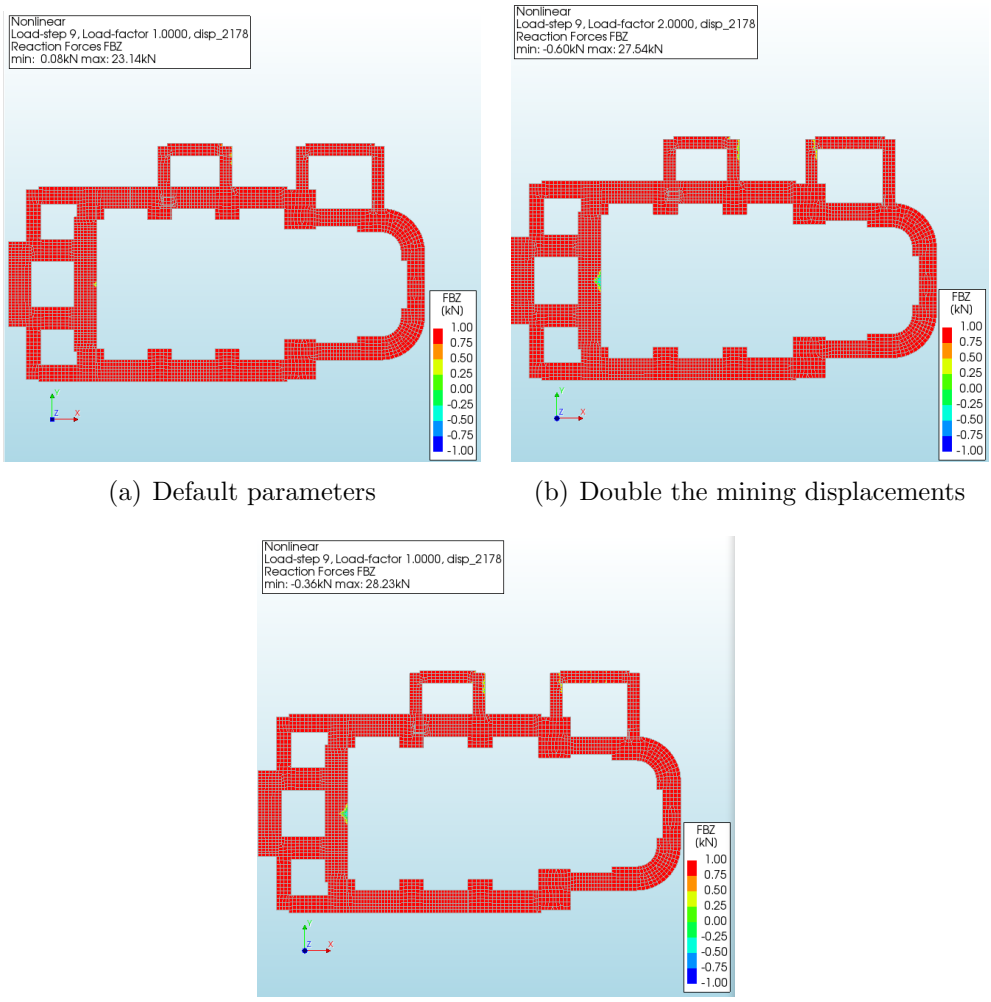

(a) Default parameters

(b) Double the mining displacements

(c) Stiffest soil-structure interaction

Figure 41: These figures validate that there is no vertical tensile reaction force occurring at the structure's foundation upon imposing the external deformations. In the figures, a positive reaction force indicates that the interface element is under compression, whilst a negative value implies tension.

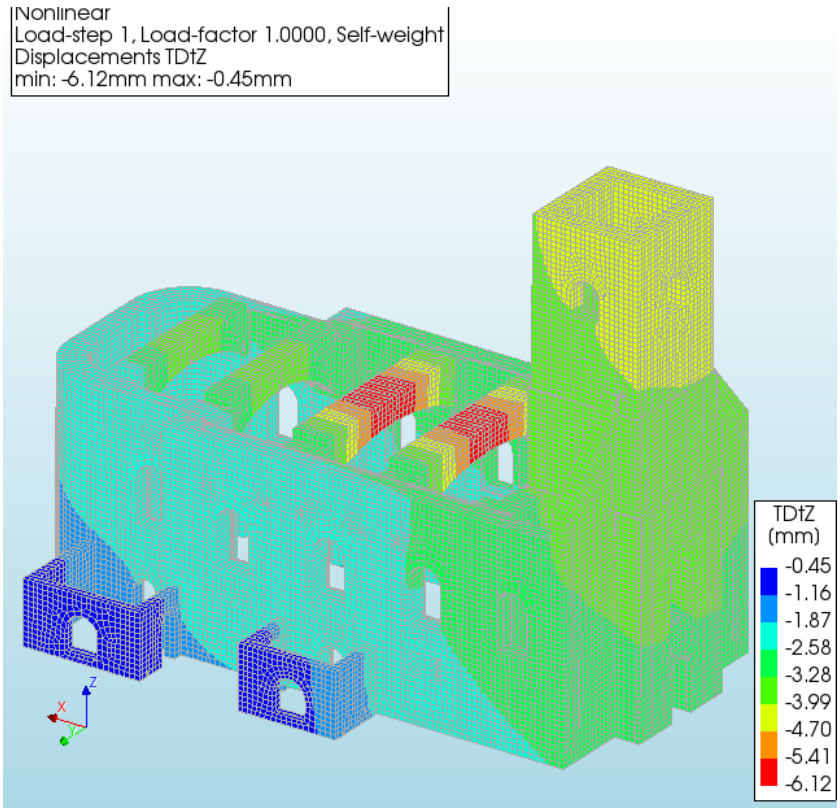

Figure 42: Vertical deformations of the church model with the parameters listed in Table 4.

at the brickwork arches, partially indicating a beam like behaviour, which will be further elaborated on when evaluating the stresses. The arches have a deflection at mid-span of approximately 4 mm over the span of 10 m relative to the ground floor.

The horizontal displacements are shown in Figures 43 and 44. Near the ground the walls displace the least. The majority of the displacements in the x-direction are at the top of the tower, leaning forward due to increased vertical displacement caused by self-weight. The majority of horizontal displacements in the y-direction (Figure 43) are observed just below the springing-point of the arches. The later displacements here can be attributed to two causes. The first is that of a beam in a solid frame, which will have the effect of bulging out connecting columns. The second is that of an arch or triangular truss with a limited tensile tie, caused by an inclined member with compressive force inducing a horizontal force. The latter is comparable to a vertical force on a cantilever beam. Both are validated when looking at the horizontal stress distributions. It is also visible that the side of the structure with the connecting annexes is stiffer than the side without. This additional stiffness is attributed to the connecting walls of the annexes, which provide a higher bending stiffness with more support (similar to a section with increased stiffness in a frame).

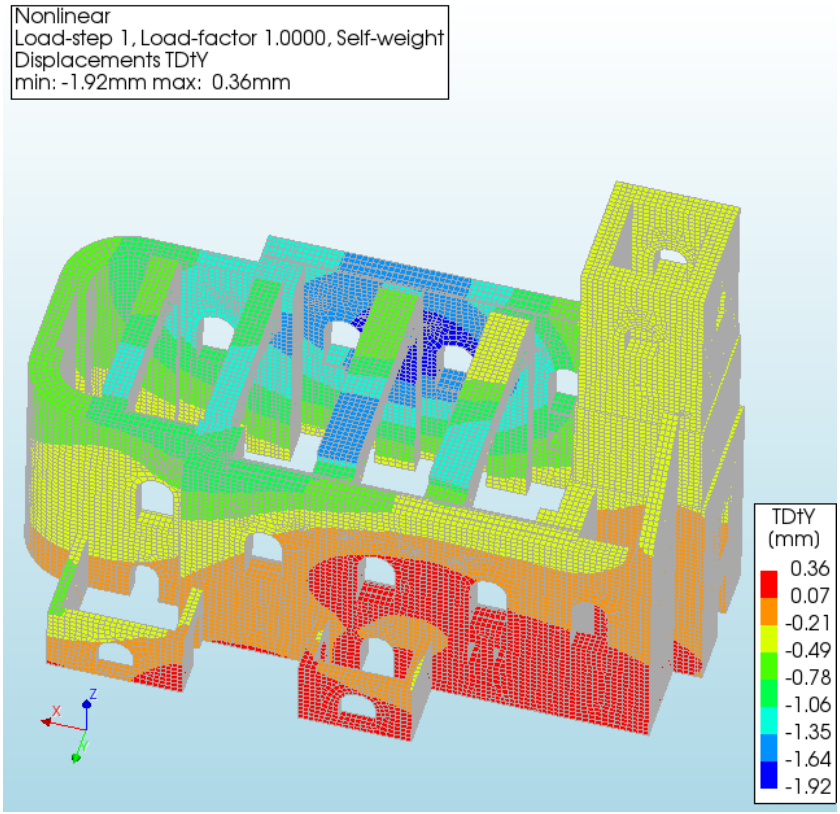

Figure 43: Horizontal deformations in the y-direction of the church model with the parameters listed in Table 4.

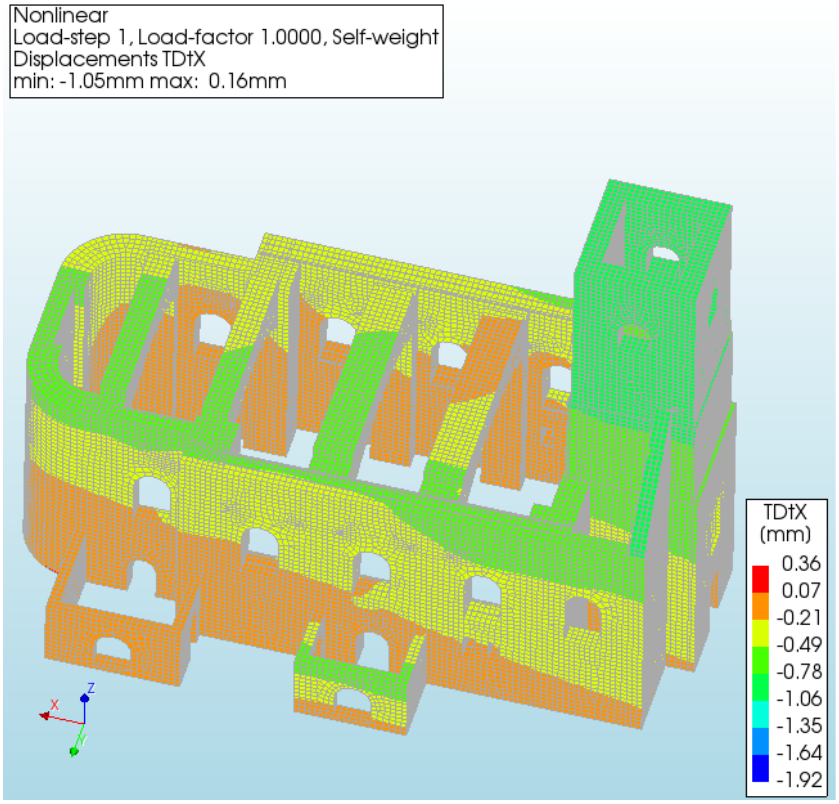

Figure 44: Horizontal deformations in the x-direction of the church model with the parameters listed in Table 4.

4.6.2 Horizontal, vertical and principle stresses

In the church's situation, the most critical stresses occur when the ultimate tensile stress is reached at 0.1 MPa (default value in Table 4). In Figure 45 the major principle stress is shown from multiple viewpoints. The figure mainly indicates high stresses at openings, the arches and annexes. At the bottom of the windows most tensile stress is the result of the vertical load being spread (Figures 45(a) and 47). The same effect occurs at the upper sections of the windows, but it is less pronounced and visible due to the curvature. The tensile regions on the outside of the outer walls above the windows and at the inner of the rear right curved section are related to the horizontal displacements in the y-direction (Figure 43). The stresses in these regions are smaller on the left of the church than on the right due to the additional rigidity provided by the annexes.

The brickwork arches are believed to be the primary concern in the church. This is supported by the fact that the reinforcement ties were added approximately two centuries after the initial construction. In Figure 46, the bending stresses of the arches and the formation of rotational mechanisms forming at the mid-span and outer supporting walls can be observed. The arches behave both as a beam in bending and an arch in compression. The beam behaviour is believed to be due to the height of the cross-section and the relatively low curvature of the arch. In terms of the loading conditions, the majority of the load can be accounted for when regarding the moment distribution, with the load being approximately 70 kN/m at mid-span to 100 kN/m near the supports. The compressive normal force at mid-span, and near the supports, however indicates the arch behaviour, which is restrained by both the bending of the outer walls (Figure 43) and the tensile force in the ties. The most loaded tie pair have a combined tensile force of approximately $90kN$ (working at less than 5% of the capacity of modern structural steel). Despite a relatively low force, the lever-arm of approximately 1.5 m, helps in a strut-and-tie model. It is also worth mentioning that without the ties, the model is unable to converge once the external deformations computed in Subsection 3.3 are applied.

The majority of vertical stresses are throughout the structure are compressive, with compression peaks at the tower or being caused by bending, Figure 47. For the remainder, the values mostly align with the present self-weight of the masonry.

4.6.3 Major principle crack width

Figure 48 shows the major principle crack width. The figure aligns with that of the tensile stress (Figure 45). Most regions show small hairline cracks. The only real exceptions are located at the mid-span and the supports of the arches, the inner tower openings and external door openings at the annexes. The largest crack width occurs at the second arch from the front (loaded with R4 and C4 in Figure 38) with a peak of 0.24 mm.

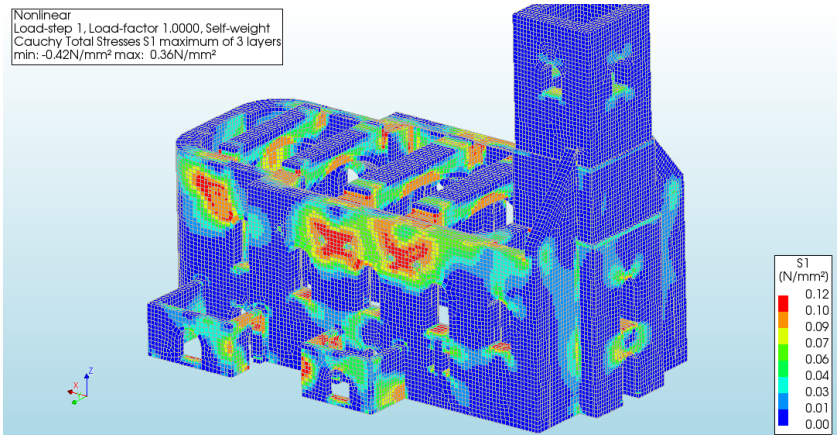

(a) Outer view on the left of the church

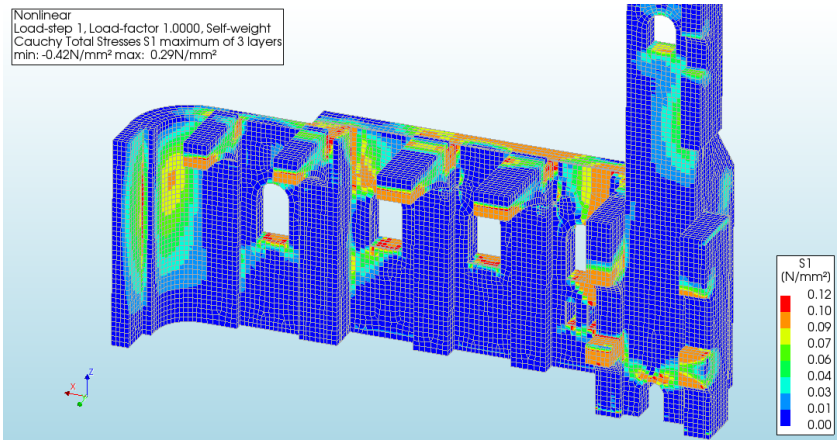

(b) Inner view

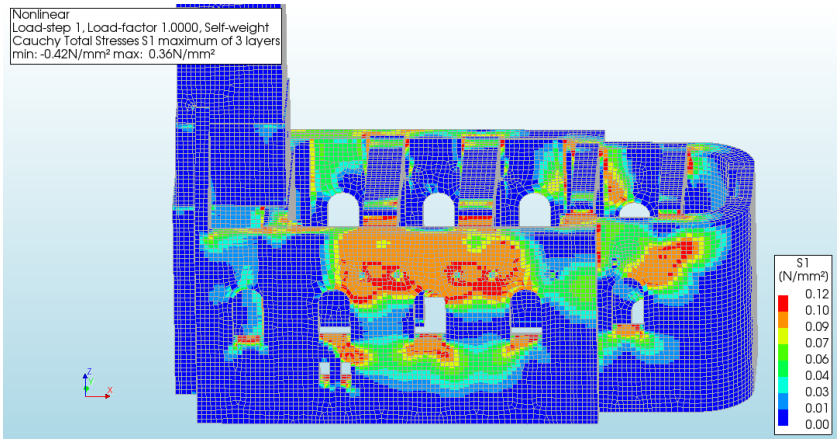

(c) Outer view on the right of the church

Figure 45: Major principle stresses (tension) of the church model with parameters listed in Table 4.

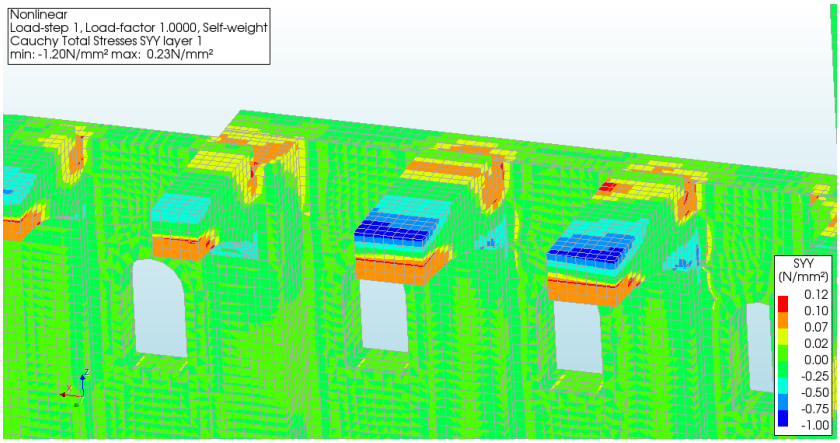

Figure 46: Normal stresses along the span of the brickwork arches, parameters listed in Table 4. In the third from the left arch, the bending moment and normal force (M, N) are ($412.7kNm$, $-555.8kN$) at mid-span, and ($-841.2kNm$, $-461.1kN$) at the support on the right outer wall (side without annexes).

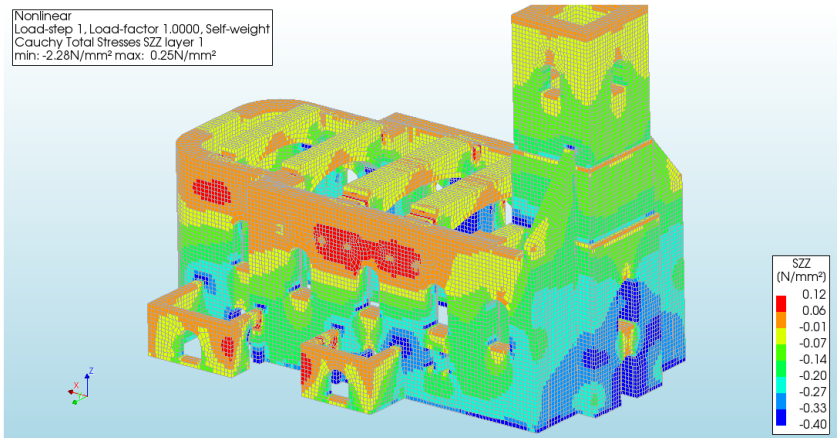

Figure 47: Vertical stresses of the church model with parameters listed in Table 4.

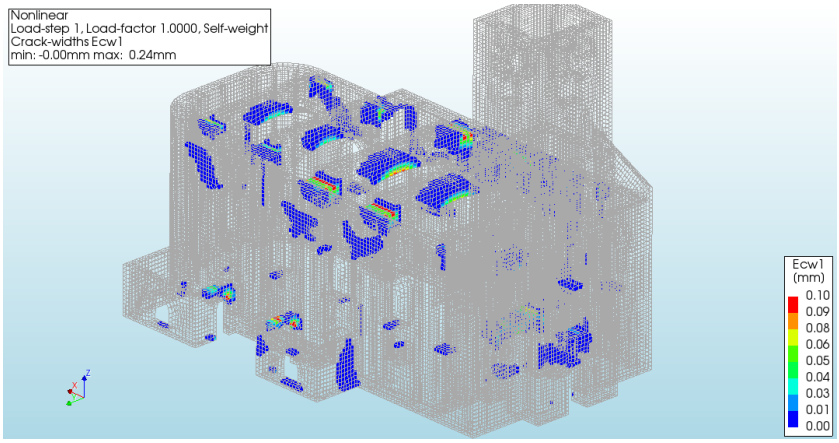

(a) Outer view on the left of the church

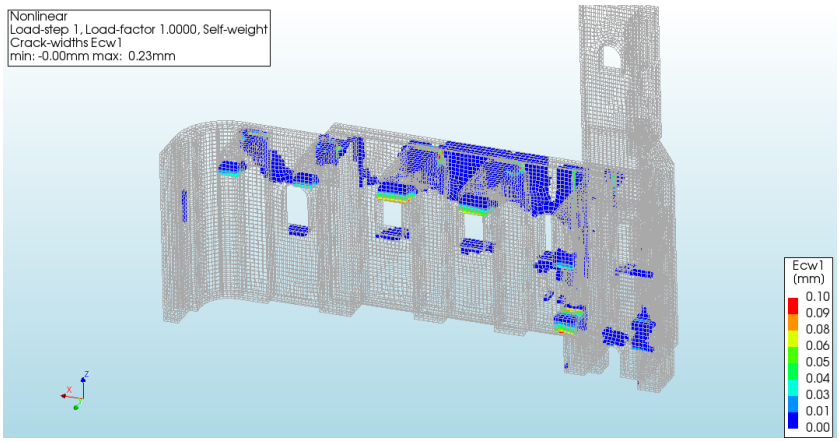

(b) Inner view

Figure 48: Major principle crack width of the church model with parameters listed in Table 4. In Figure 48(b) the outer wall cracks are on the outer surface, with exception of the cracks in the inner rear curved section. The boundaries of the legend is limited to 0.10 mm, to still identify a gradient in most cracks. The peak of 0.24 mm is located at the brickwork arches.

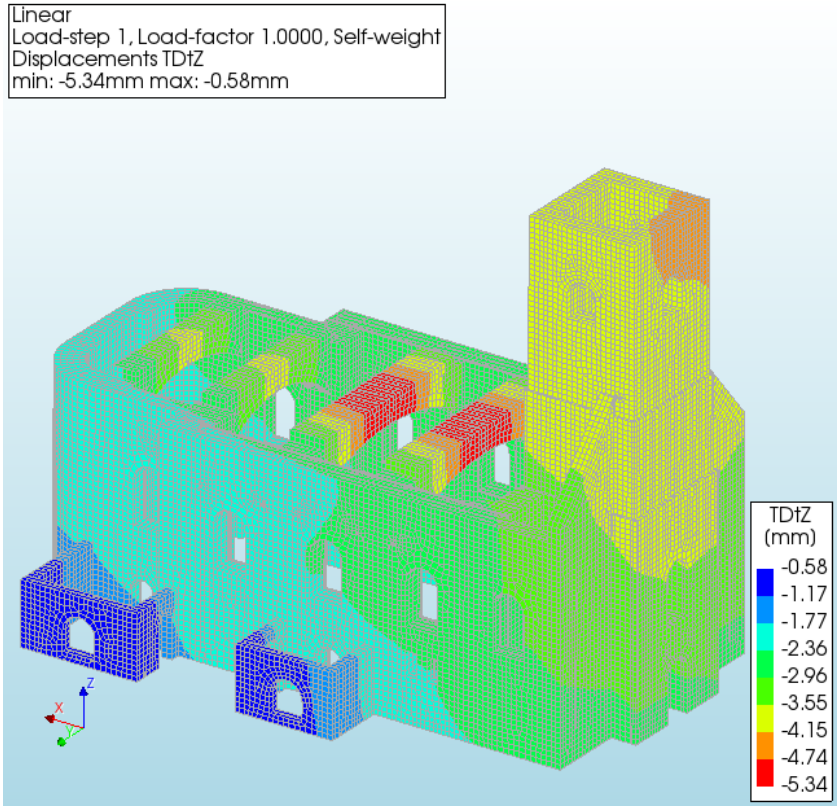

Figure 49: Linear elastic vertical deformations of the church model with the parameters listed in Table 4.

4.6.4 Comparison with linear elastic analysis

The advantage of performing a nonlinear analysis shows when comparing the vertical and horizontal deformations. Figures 42 and 43 are nonlinear, and Figures 49 and 50 are the corresponding linear elastic counterparts. The linear elastic model appears to be stiffer, with the deformation range of the vertical displacement increasing 10% and the horizontal 20%. Most of the difference is related to the internal forces at the brickwork arches, both vertical and horizontal displacements. The nonlinear material allows for vertical plastic deformation due to the formation of hinges (shown in Figure 46). In addition, the nonlinear model indicates a reduction of flexural stiffness of the right outer wall, which results in more horizontal deformation when compared to the linear elastic model. This can also be seen in Figure 50 with the difference in the displacements of the left wall above the connection of the front annex. In this case, the left wall bulges more in the nonlinear model.

The major principle stresses in both linear and nonlinear are similar. Regions of high tensile stress are well identified in the linear elastic model, Figure 51. With the peaks being lower in the nonlinear model.

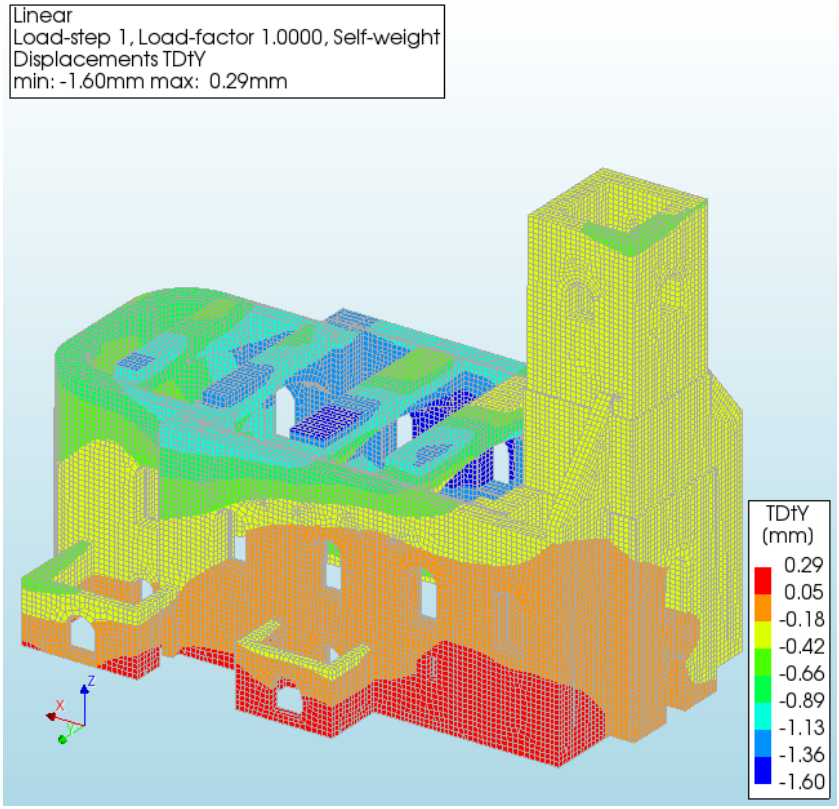

Figure 50: Linear elastic horizontal deformations in the y-direction of the church model with the parameters listed in Table 4.

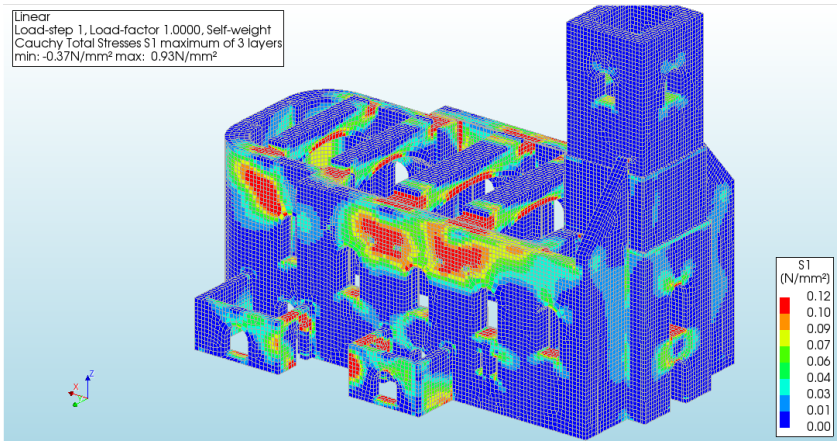

Figure 51: Linear elastic major principle stresses (tension) of the church model with parameters listed in Table 4.

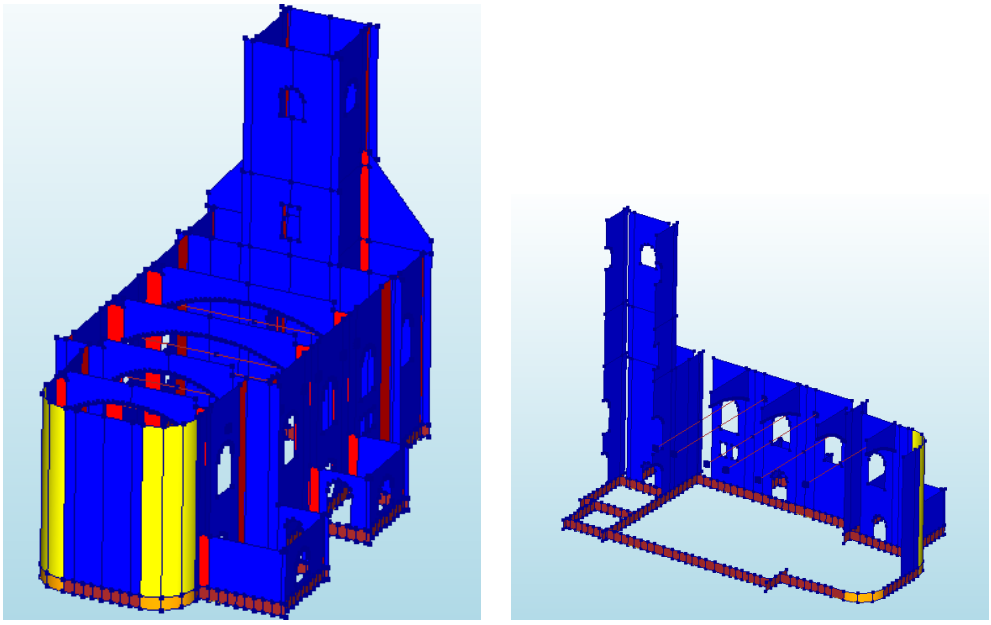

(a) Full model (b) Partial model

Figure 52: Shell model of the geometry. Blue/yellow represent masonry walls, red shells indicate additional wall sections required for connectivity, dark-orange shells are the foundation walls and red lines represent steel ties (visible at arches). A similar Figure has been created for the solid element model, Figure 37.

4.7 Response to self-weight using shell elements

In this section, the same church structure has been created using shell elements, and only the response to the self-weight has been evaluated. This is done to validate the observations in the solid elements model, and highlight some of the advantages and disadvantages of using solid elements. A virtual representation of the shell element model is shown in Figure 52, which is established using the geometry in Figure 53.

4.7.1 Vertical and horizontal deformations

The deformations of the shell structure are very similar in behaviour to those of the solid element model. Especially vertical displacements, shown in Figure 56, and global interaction between larger regions are near identical. However, some local differences can be observed in the horizontal displacements. In y-direction (along the width of the church), shown in Figure 54, the out-of-plane bending in the outer walls varies. This can be due to the differences in the input and method in which the arches are connected. Another possible reason for this difference can be due to the assumptions made in the applied theory. DIANA for the curved shell elements assumes normals remain straight ("straight needle hypothesis") with zero normal stresses. Both assumptions are questionable if the thickness is significant, as is the case in this situation, where generally the walls are more than 1 m thick with some sections even reaching 2.4 m. In x-direction

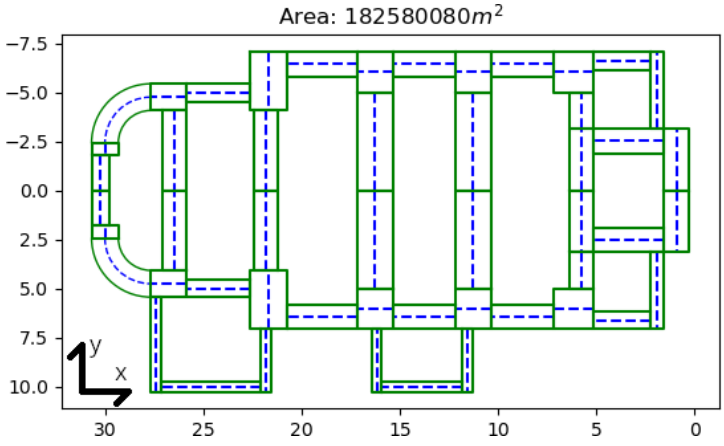

(a) Solid elements

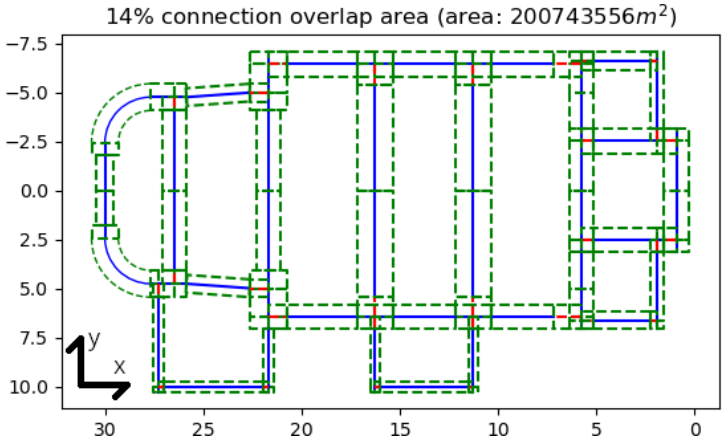

(b) Shell elements

Figure 53: Indication of changes in geometry input, comparing solid and shell elements. In the shell element model, all centre-lines connect with each other; this causes overlap. These sections are represented by the dashed red lines and are lines that have been added to create connectivity. In addition to the overlap for connecting, certain sections have been simplified and walls have been shifted slightly to simplify the input. Most notable are the brickwork sections on which the arches (spanning in the width or the y-direction) are less stiff on the shell element model. Other sections include the slight shifts in the annex walls, the wall connecting the left annex to the main structure and the shift in the rear wall (far left).

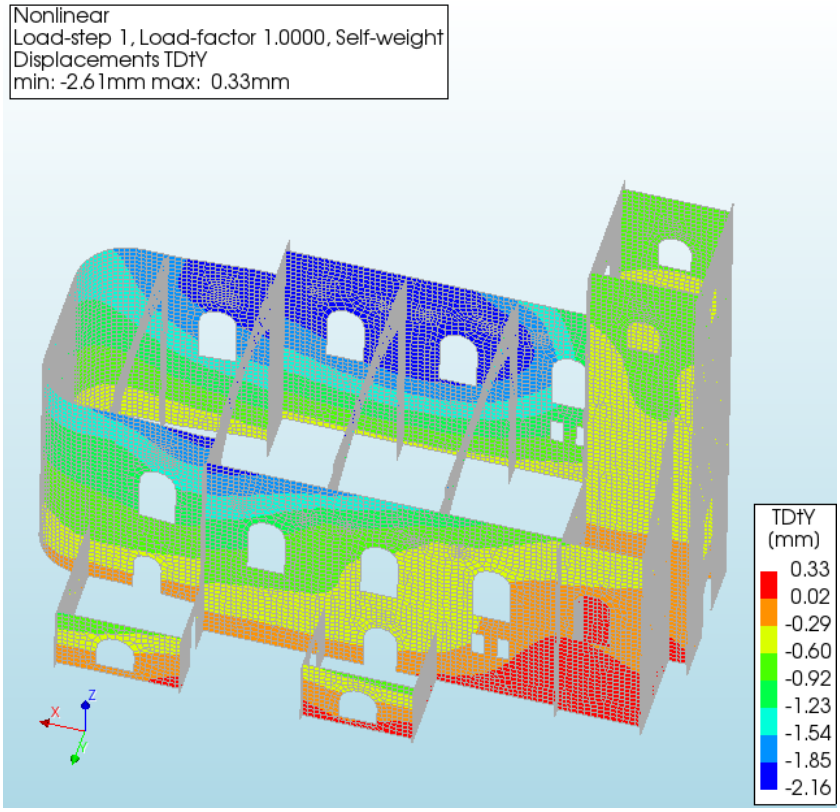

Figure 54: Horizontal deformations in the y-direction of the shell model with the parameters listed in Table 4, to be compared with Figure 43.

(along the length), shown in Figure 55 the most notable differences are the transitions at the rear-right of the church (upper-left in Figure 53). In the rear-right the curve is pulled straight by the deformations in the y-direction, most visible at the windows. In the shell element model, this effect is more pronounced. This is a consequence of the assumptions made in the applied theory relating to bending, but also in the sudden transitions in the shell model and slight changes in input geometry.

4.7.2 Tensile stresses and crack width

The tensile stress regions, in Figure 57, of the shell model, with the exception of the connecting elements and ties are very similar to those observed in the solid element model. This trend is also observed in the crack width response of the shell model, shown in Figure 58.

4.7.3 Discussion

Bar some slight differences in the actual output values, both solid and shell elements models return very similar results, indicating the geometry input is likely to be correct. Depending on the context a choice can be made to use shell elements instead of the

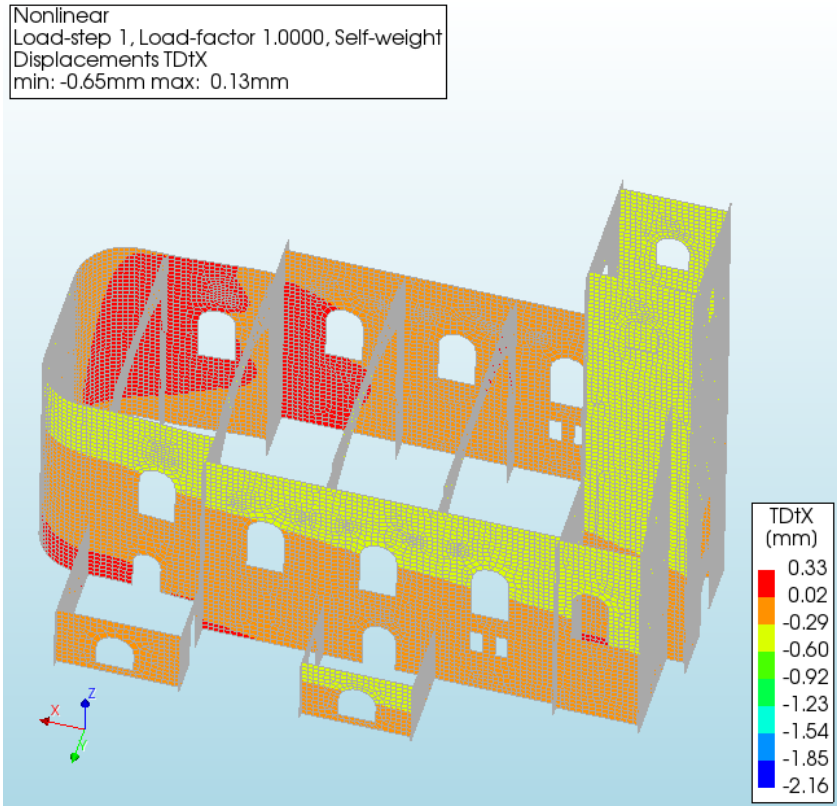

Figure 55: Horizontal deformations in the x-direction of the shell model with the parameters listed in Table 4, to be compared with Figure 44.

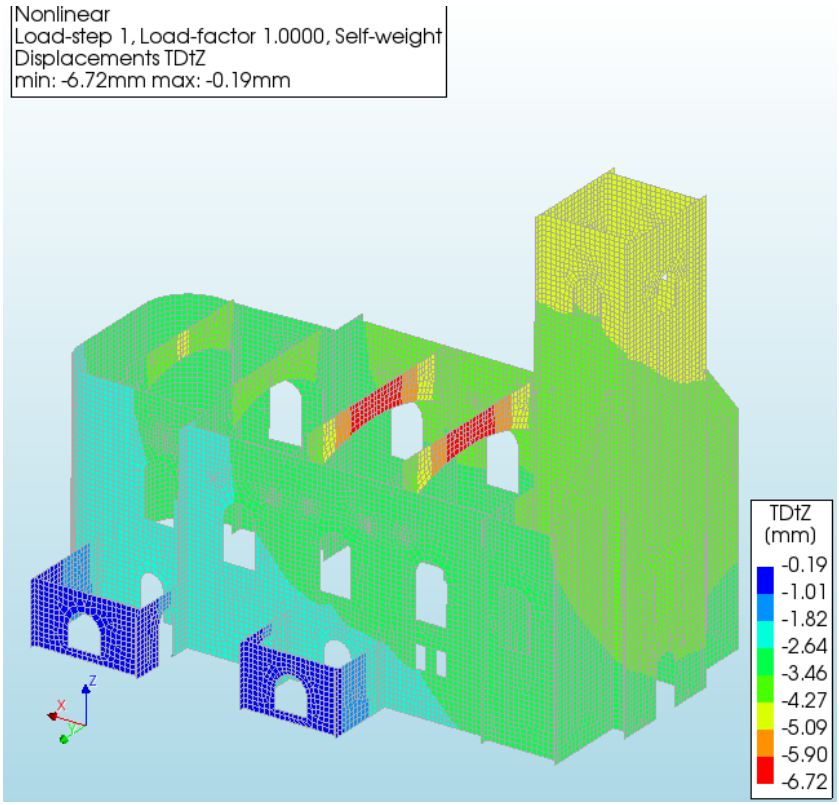

Figure 56: Vertical deformations of the shell model with the parameters listed in Table 4, to be compared with Figure 42.

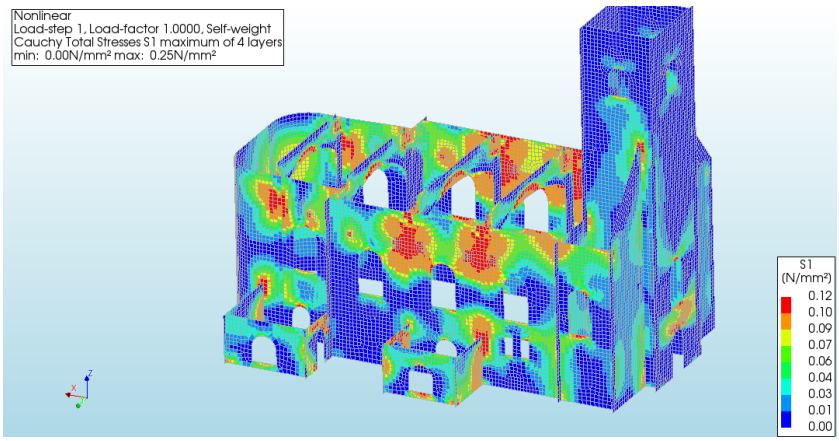

(a) Outer view on the left of the church

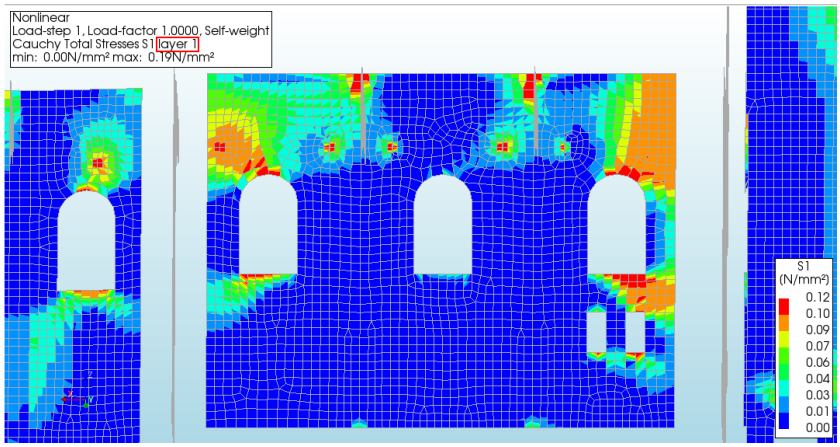

(b) Inner view of the inner layer

Figure 57: Major principle stresses (tension) of the shell model with parameters listed in Table 4, to be compared with Figure 45. Subfigure 57(a) shows the maximum of all layers, to show better similarity with the solid element model Subfigure 57(b) has been added.

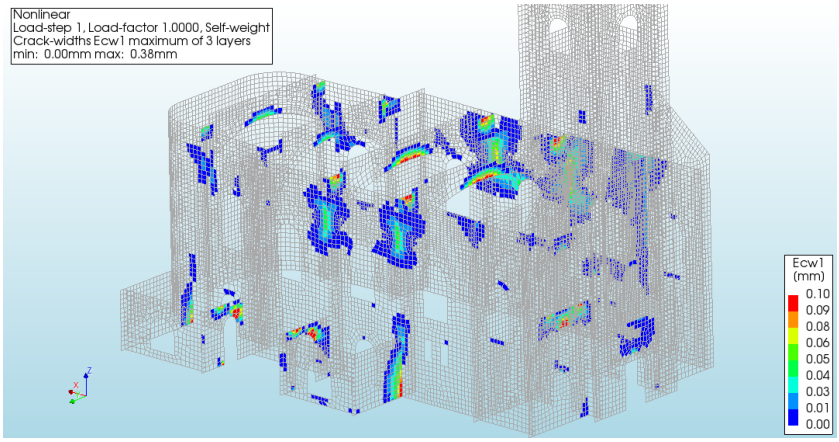

Figure 58: Major principle crack width of the shell model with parameters listed in Table 4, to be compared with Figure 48. In this figure, the maximum of all shell layers is plotted. The boundaries of the legend is limited to 0.10 mm, to still identify a gradient in most cracks. The peak of 0.38 mm is located at the brickwork arches.

more computationally expensive solid elements. For determining the locations of stress regions and global response shell elements are sufficient. On the other hand, the shell element model falls short when interested in out-of-plane deformations or information at the transitions. In the remaining sections, the decision has been made to discard the shell model and continue running the solid element model.

5 Model integration and assessment

The final step is to integrate the interpolated deformations with the structural model, and analyse the results. In relation to the damage, this section predominantly focuses on cracks that develop as a response to the loading. These cracks can be compared to visual inspections or with prior renovation reports.

The section has been divided into four subsections. The first presents the structure's response upon imposing the deformations computed in Subsection 3.3. After which, two subsections are devoted to the sensitivity analysis of both the structural parameters and the input deformations. Then, the results are discussed and compared with what is known about earlier occurring damage.

5.1 Response to the estimated deformations

In this analysis, deformation data spanning from December 2014 till December 2020 has been used. Any prior deformations are assumed to have been zero, as there is no clear trend or information to extrapolate them with. The estimated deformations are applied to an interface layer below the foundation level, discussed in Subsection 4.5. These deformations have been inputted as incremental load steps.

Both vertical and horizontal deformations are applied to the structure. Figure 59 provides an overview of the magnitude of the differential settlements over time and the load dates used during the analysis. The figure suggests that most deformations occur in the first two years.

Figure 60 shows the deformations at the foundation level of the church on the most critical load date. This date matches with the peak of the input (Figure 59), which also occurs after 816 days. The horizontal deformations are predominantly along the x-axis (length direction). This is because the method only observes West-East movement, which is most aligned with the x-axis. The tower is being pushed inwards due to the horizontal displacements, as shown in Figure 60(a). This trend doesn't change over time. In the vertical direction, the front section containing the tower, settles the most with a linear slope towards the rear, as seen in Figure 60(c). Along the width direction, the vertical difference is approximately 3 mm, which is not clearly visible in Figure 60(c). It can, however, be established using Figure 25 in Section 3.

Figures 61 and 62 display the increases in the tensile strain due to the deformations. The church, excluding the brickwork arches, is most affected by the horizontal displacements shown in Figure 60(a). It is clear that the tower indeed is being pushed towards the rear of the structure. This is supported by the bending of the front facing wall, and the triangular shapes of the strain in the tower walls and outer walls.

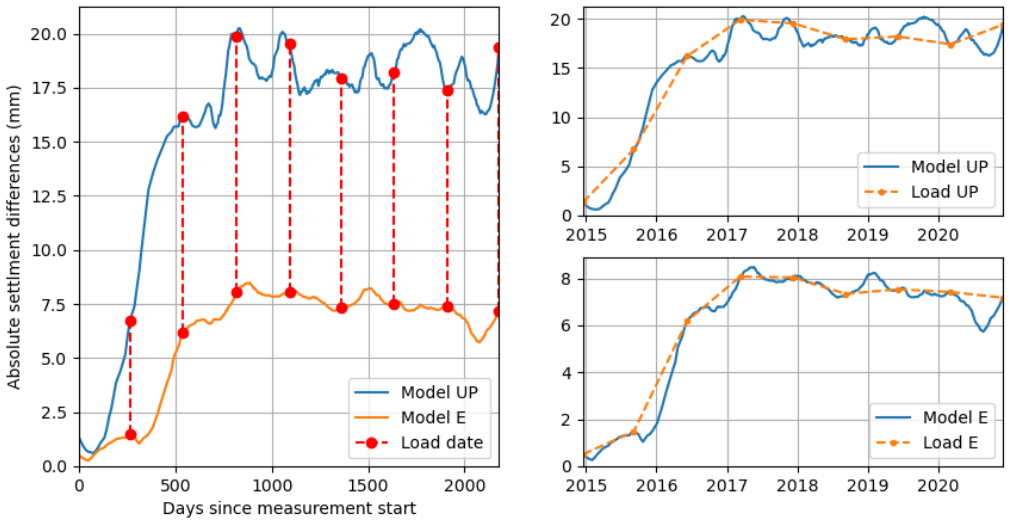

Figure 59: This figure represents the load dates introduced to the structural model. The plots represent the absolute largest observed difference in the input deformations at a given time. In the left plot, the dots represent the dates chosen to be inputted. The dashed line in subplots on the right show the loading path followed by the finite element software, DIANA FEA when performing the analysis. In other words, both Up and East models are approximated by the dashed lines upon input.

Figure 63 shows the major principle crack width at both the initial self-weight condition and the final deformation state. Most new cracks occur only when including both horizontal and vertical deformations. The vertical displacements only appear to be of significance at the brickwork arches.

5.2 Sensitivity of the response to structural parameters

In the structural analysis, there are six quantifiable variables shown in Table 5 and a change in the tensile softening curve from linear to exponential. Each value is altered individually, and variations in the cracks are assessed.

Property	Unit	Minimum	Maximum	Default
E (masonry)	GPa	1	6	3
Tensile strength	MPa	0.06	1	0.1
Fracture energy	N/mm	1	50	5
Masonry density	kg/m^3	1800	2000	1900
Vertical interface stiffness	MN/m^3	5	190	95
Horizontal interface stiffness	MN/m^3	20	95	47.5

Table 5: Quantifiable variable structural properties used in the sensitivity analysis.

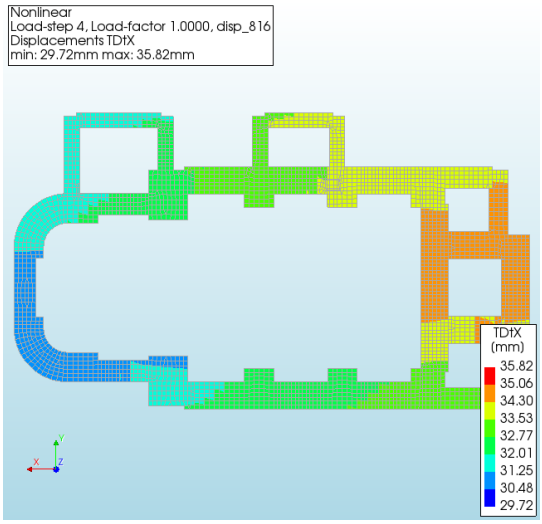

(a) x-direction

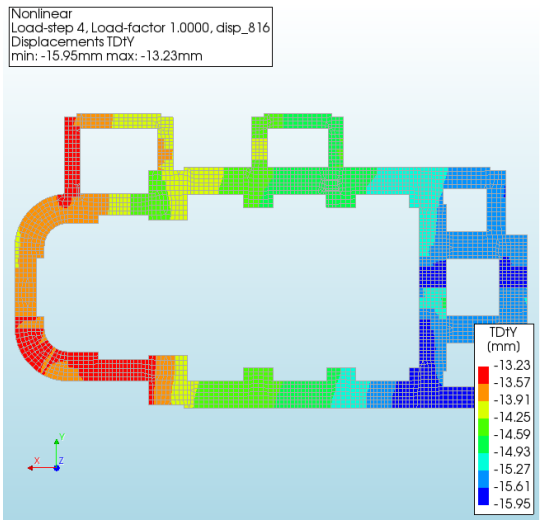

(b) y-direction

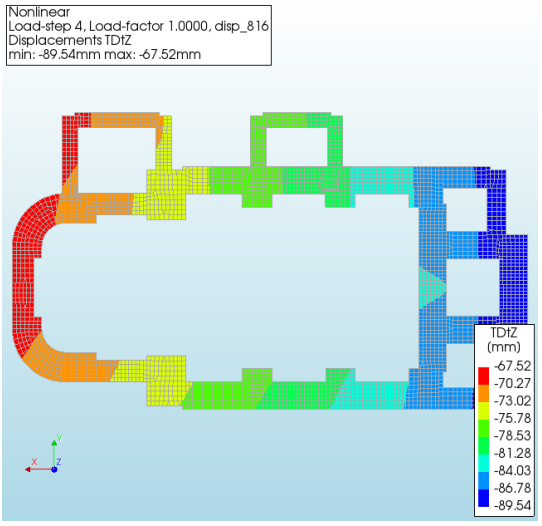

(c) z-direction (up)

Figure 60: In these figures, the response at the bottom of the foundation is shown. The peak for both horizontal and vertical displacements occurs after 816 days. Each includes the deformations caused by self-weight, which is why they deviate slightly from the input in Figure 59. The z-direction indicates an upwards motion when positive. Hence the lowest value indicates the most settlement.

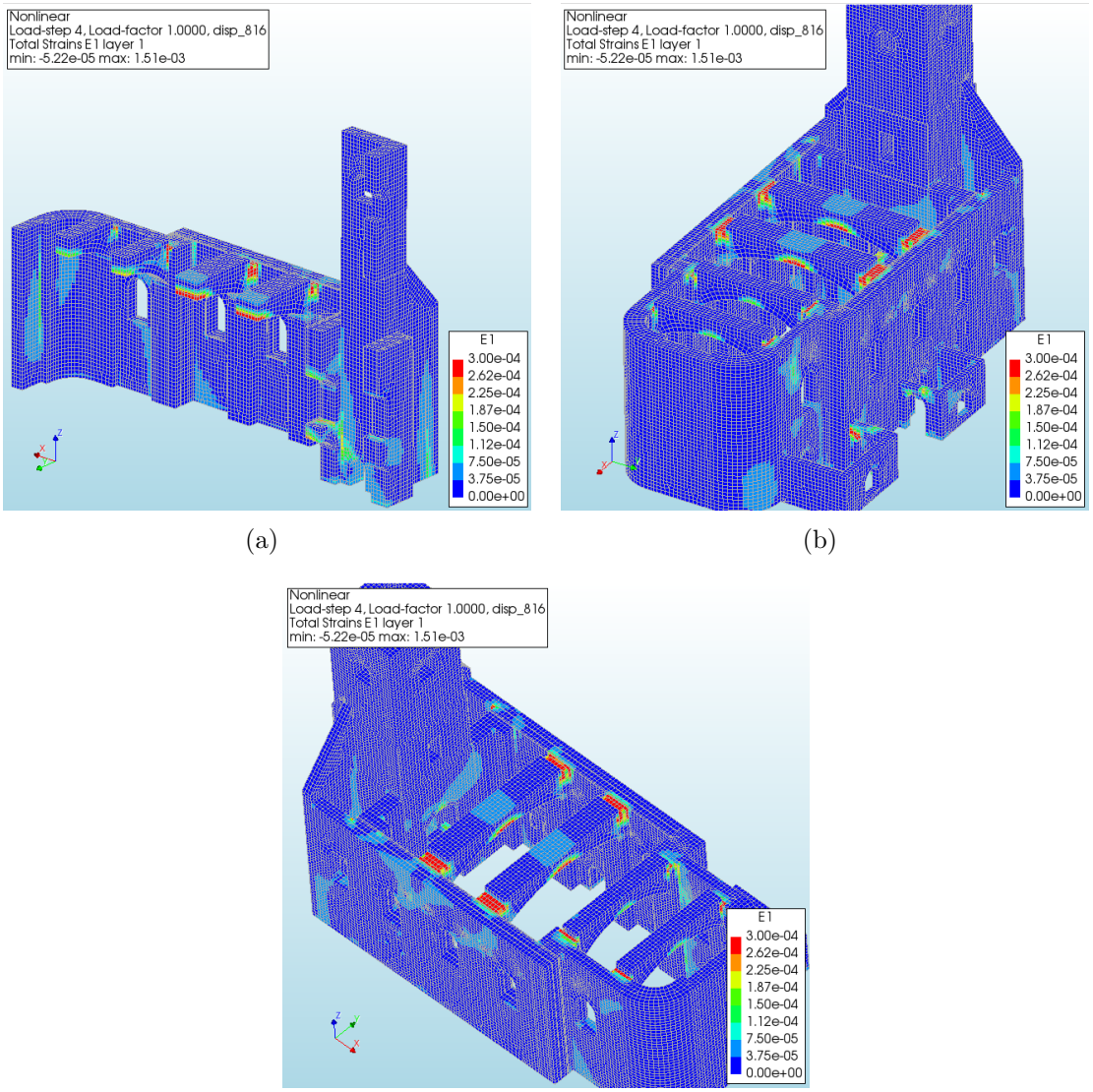

Figure 61: In these Figures the additional total strain, not including the strain due to self-weight, after 816 days of measuring deformations is shown. 816 days is the load date with the most horizontal and vertical displacement difference. All Figures show the major principle total strain, highlighting the regions in which tension is dominant. The choice of the scale is set to $3 \cdot 10^{-4}$, which is the ultimate tensile strain.

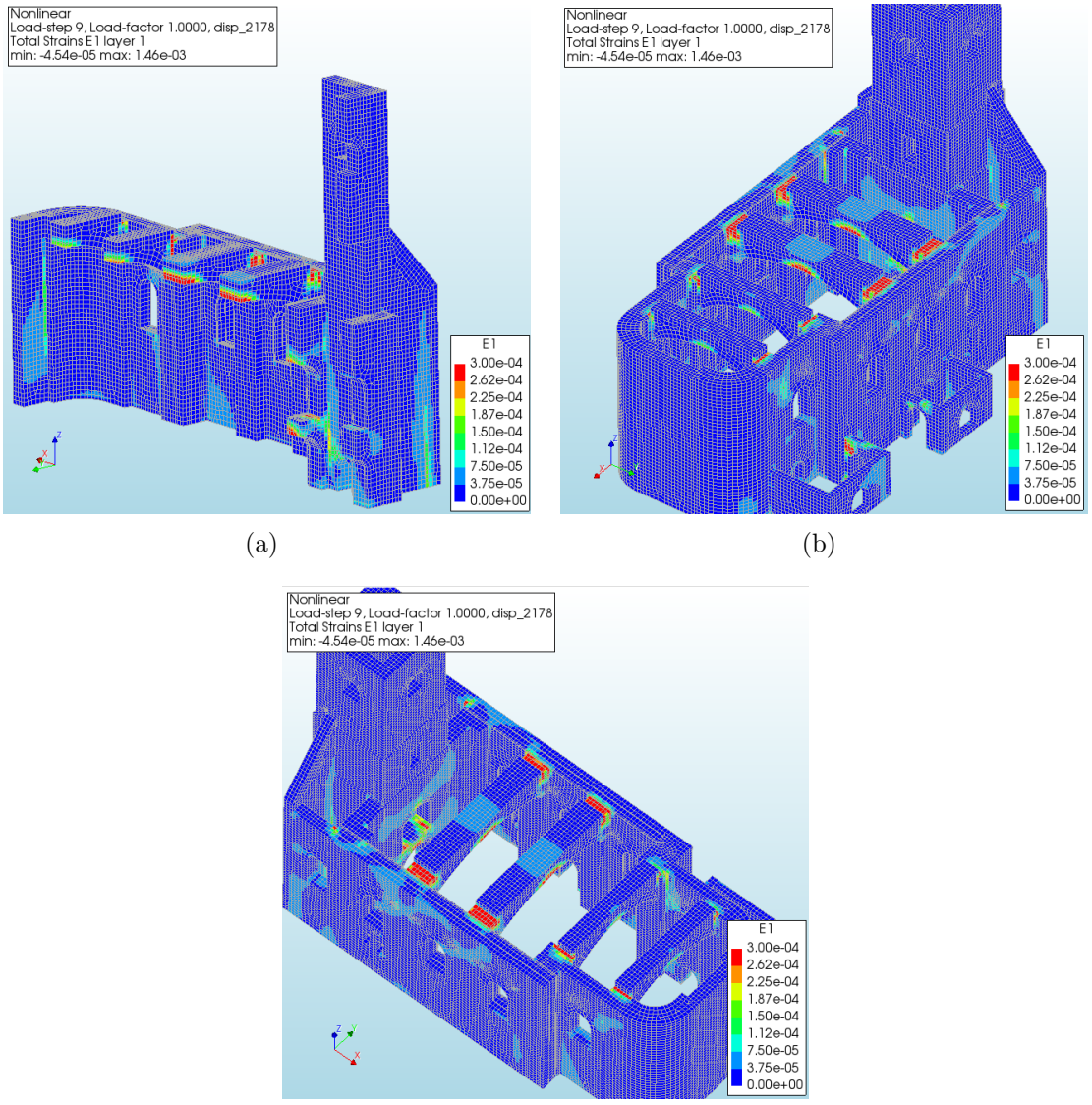

Figure 62: In these figures, the additional total strain at the final observation date are shown, not including the strain due to self-weight. They all display the major principle total strain, highlighting the regions in which tension is dominant. The choice of the scale is set to $3 \cdot 10^{-4}$, which is the ultimate tensile strain.

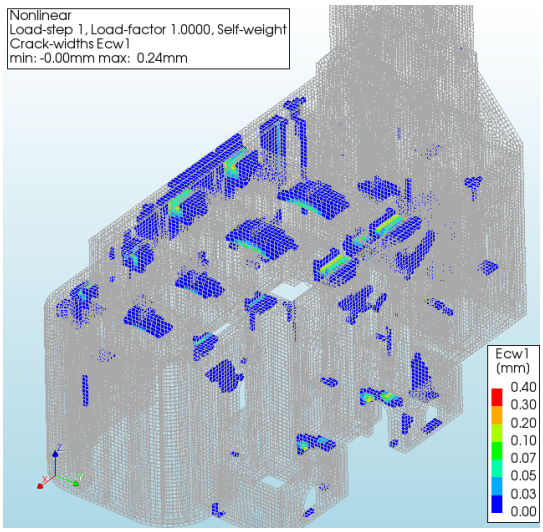

(a) Without deformations

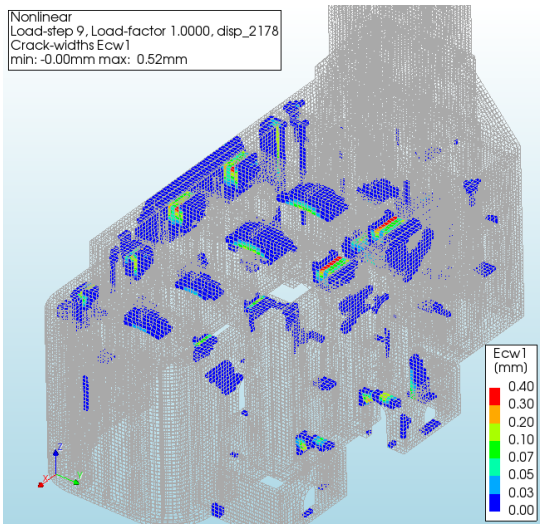

(b) Only vertical deformations

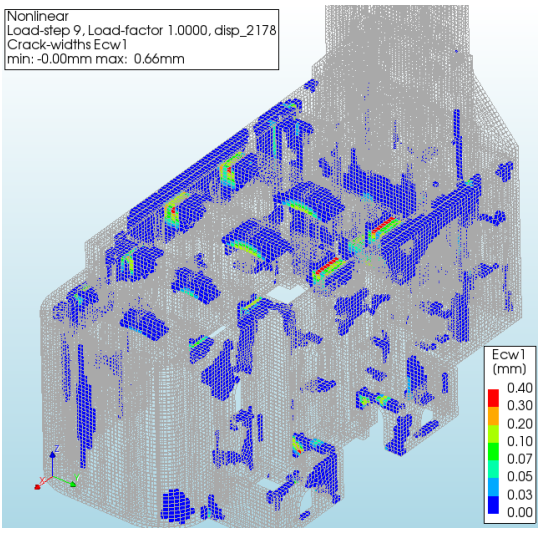

(c) Both horizontal and vertical deformations

Figure 63: In all three figures, the total major principle crack width is shown, which includes the response to self-weight. Figures (a) and (b) are nearly identical, with the only key differences appearing near the arches. Figure (c) contains significantly more cracks, indicating that the horizontal deformations affect more sections of the church.

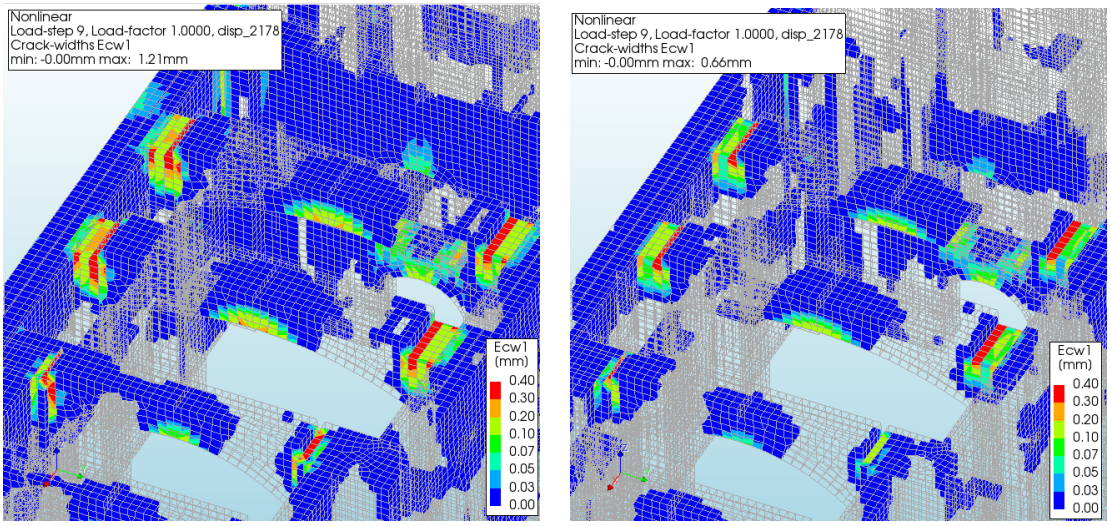

(a) 0.06 MPa (b) 0.1 MPa

Figure 64: In these Figures, the effect of the tensile strength is shown using the major principle crack-width. Figure (a) has a larger value in general at the arches and the effected regions are larger when compared to (b).

5.2.1 Fracture energy and curve

Softening allows the element to gradually reach a point of zero stress as the strain exceeds the ultimate tensile strain. The appropriate value is typically hard to establish. An element size of approximately 250 mm has been used in the structural model. The range considered for energy ranges between 0.1 and 50 N/mm.

When varying the value, no changes can be observed to the crack-width among the considered values. The same observation can be made when comparing linear to exponential softening (section 4.4).

5.2.2 Tensile strength

The tensile strength relates to the ultimate principle stress. When exceeded, a crack is formed. High values result in a model which behaves similar to a linear elastic analysis, previously discussed in the response to self-weight. Lowering the value results in more and larger cracks. The lowest value that can be adapted for the tensile stress in the model is 0.06 MPa; at this point, the brickwork arches appear to fail at the supporting columns. For illustration, Figure 64 shows the effect on the brickwork arches.

5.2.3 Young's modulus (brickwork)

In the majority of the structure, the brickwork material behaves linear elastic. Changing the Young's modulus affects the structure in two main ways. The first is generally allowing the structure to be stiffer or weaker. In general, all the deformations scale nearly one-to-one with the change in the stiffness. This also has a relation to the cracks, since the applied loads are deformations, the structure behaves more flexible, reducing crack-width. Doubling the stiffness approximately halves the peak deformations, and vice versa, a decrease increases the displacements. The second relates to the interaction between components. In the event of a reduction of stiffness, the steel ties appear more active, which slightly alters the arches' behaviour. With 30% of the stiffness, the normal force in the steel ties increases by $\approx 18\%$. On the other hand, doubling the stiffness doesn't affect the ties as much but places more importance on the annexes. More cracks appear at the annexes when the stiffness is increased.

5.2.4 Soil interface stiffness

Changing the soil stiffness affects the structure both in terms of deformation loading and the response to self-weight. Since the deformation loads are applied below the interface connecting to the church's foundation, the lower the value, the lower the force on the structure's walls. In addition, when decreasing the stiffness, the structure is more prone to settle due to pre-existing loads present in the structure, in this case, the self-weight. As previously discussed, the majority of the cracks appear to be due to the self-weight of the structure. One of the consequences of reducing the soil stiffness is that the settlement differences between the front and rear sections of the church increases, due to the weight difference. This causes the walls along the longitudinal direction to strain more, thus leading to cracks and being less favourable. Also, along the width, the displacements vary with the additional support from the annexes. Both can be observed in Figure 65.

5.2.5 Masonry density

The masonry density is only relevant to the weight of the structure. In general, the structure is more than able to bear its own weight and changing this value has no visible effect. The only exception is the weight of the ceiling, which is carried by the brickwork arches. However, even at the arches, a slight increase from 1900 to 2000 kg/m^3 has a negligible effect.

5.3 Sensitivity of the response to an increase of deformations

The last sensitivity analysis that has been performed is on the change of input deformations. In this subsection, the inputted deformations of Figure 59 are scaled by a factor of 2 and differences are discussed. Increasing the deformations allows to better highlight

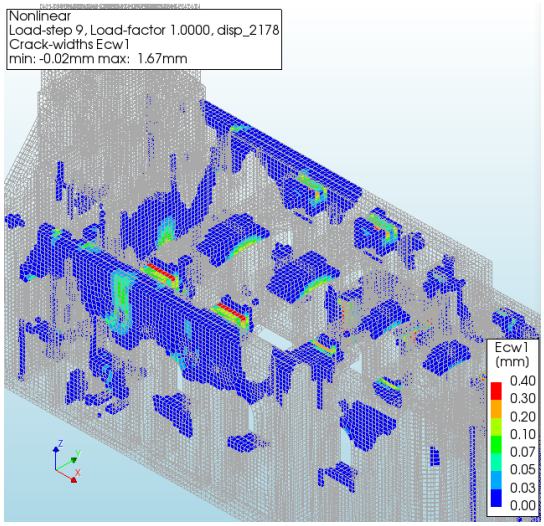

(a) Weakest soil (20.0 MN/m^3)

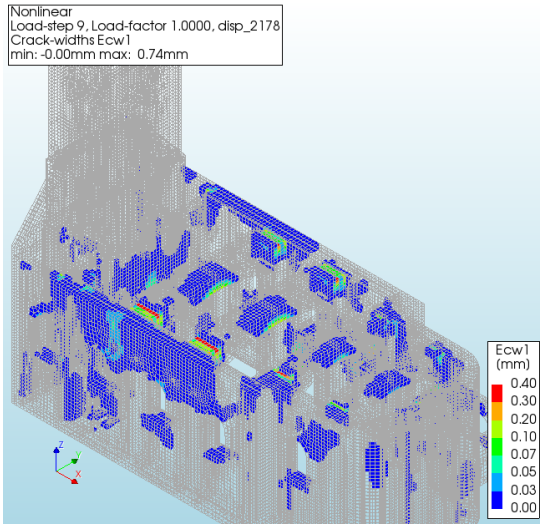

(b) Weaker soil (47.5 MN/m^3)

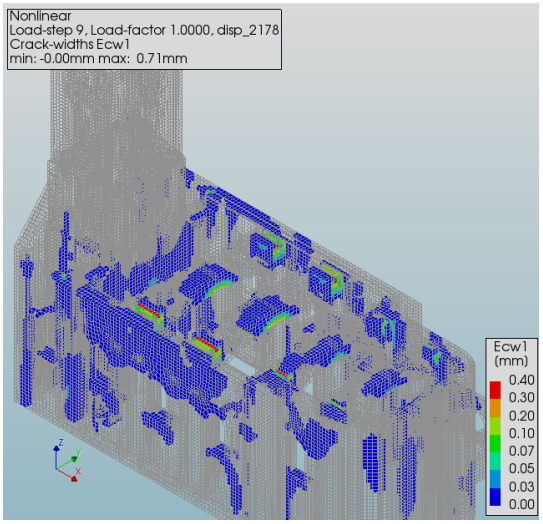

(c) Strongest soil (195 MN/m^3)

Figure 65: In these figures, the effect of the soil stiffness is shown using the major principle crack-width. In both cases, the stiffness value refers to the vertical stiffness, and the horizontal is always set to half that of the vertical. In these figures, the lower stiffness results in more cracks towards the top of the walls, whilst the higher stiffness shows the cracks due to particularly the horizontal deformations better. The horizontal deformations mainly influence the lower sections of the church and the walls near the tower.

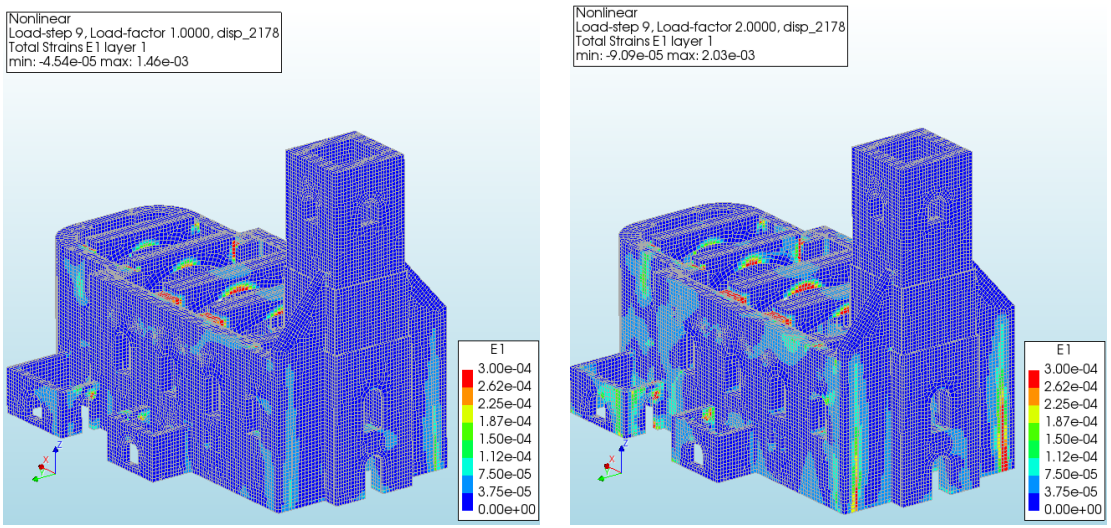

(a) Default displacements (b) Double displacements

Figure 66: The figures above show the total strain resulting from the imposed deformations. The strain due to self-weight is subtracted from the results. Figure (a) is compared with Figure (b) to get an insight into the effects of the deformations and what changes.

changes. Figure 66 shows the overall increase of tensile strains as the displacements increase. With a doubling of the displacements lower sections of the structure appear to be more affected.

5.4 Discussion

This subsection discusses the first two subsections in more depth.

Response to the estimated deformations
The MT-InSAR deformation data can be projected to vertical and West-East motion. Most cracks across the structure occur when accounting for the horizontal displacements, whereas the vertical displacements only affect the brickwork arches. However, horizontal displacements have an intrinsic limitation with InSAR, namely that deformations along the North-South are unknown. In this case, those deformations are assumed to be zero. This assumption is likely invalid, but it is the only one that can be made without more context of the displacement directions. The vertical displacements would have more effect in two cases. The first is if the magnitude of the curvature along the length of the church is greater. In which case, more cracks in the top or bottom of the nave walls would develop. The top would be more vulnerable, given the openings of the windows and distance from the supporting boundaries. The second is when the differential displacement between the left and right-hand nave walls increases, making the brickwork arches more critical.

In a previous renovation report of March 2015, right at the start of the MT-InSAR observation period, curvature along the longitudinal direction was stated to cause cracks. These cracks occurred near the window openings, and inserts of the windows had to be replaced. In addition, cracks have been reported at the door arches and lower openings. In this analysis, cracks occur at the door arches, specifically near the entrance, and they are attributed to the horizontal displacements.

Sensitivity of the response to structural parameters

Of the structural parameters, three stand out, namely the tensile strength, Young's modulus and simplified soil stiffness. The tensile strength influences the cracks the most; this is expected as it directly determines at which stress a crack is formed. The Young's modulus and soil stiffness determine the relative stiffness difference of the church's structural components (tower, nave walls, annexes and brickwork arches). The Young's modulus can vary the connectivity between the annexes and the main nave. The soil stiffness changes the settlement differences between the tower and annexes with the nave. Additionally, it affects how much the soil deformations influence the structure. For this simplified model, the horizontal stiffness is assumed to be half that of the vertical. Changes between the relation or accounting for nonlinear behaviour could alter the horizontal displacements' influence.

6 Conclusion and recommendations

The main objective of this thesis is to integrate deformations, as a result of mining, obtained using radar interferometry, with a structural model of a church. The area surrounding the church showed significant horizontal and vertical displacements. Despite the significant deformations, not a lot of curvature has been observed in the vertical displacements. In the structural model, most cracks result from the applied self-weight or horizontal displacements. To conclude the thesis, the initial research questions are discussed.

How to obtain deformations from an MT-InSAR analysis for integration in a structural model?
Interpolation was done using two different approaches: a least squares (LSQ) method with a polynomial shape function and Ordinary Kriging. Kriging has been performed on a larger scale than the least squares method. It obtains information about the approximate shape and gains insight into the displacements surrounding the church region. Only the least squares method has been used to interpolate the deformations for the structural model of the church.

To perform Kriging interpolation, one needs to obtain a reliable variogram. In this situation, just over 150 persistent scatters have been included in the variogram computation. This requires the region that has been considered to be relatively large when compared to the church. As a result, it is influenced by points at larger distances, making it less favourable than LSQ when determining points at the structure.

The least squares approach has been applied to 21 persistent scatters near the structure. With 10 coefficients for the polynomial fitted by the least squares, the method can obtain a best-fit, potentially reducing some noise in the individual point displacements. It also establishes a general trend that is believed to be more representative of the soil deformations. In future use cases of the approach, it is recommended to establish the estimation error in the MT-InSAR analysis, to propagate the error in the LSQ model.

During the six-year observation period, the church has a differential vertical settlement of approximately 20 mm and 8 mm along the West-East direction. Of these differential settlements at the church, predominantly the linear terms of the polynomial play a role. Over 80% of the vertical displacements and virtually all the horizontal displacements are accounted for by the linear terms.

How to integrate the displacements and model a building?
The church has been modelled using a nonlinear finite element model using solid elements. This type of model permits nonlinear material properties, which have been applied to analyse the crack-width, representing the visible damage. The soil-structure interaction allows differences in the interpolated displacements and those directly beneath the church's foundation.

During a linear elastic analysis, it has been observed that the stiffness is greater, specifically at connections and regions where cracking occurred. In the case of shell elements, the connectivity between walls, transitions in thickness and out-of-plane bending, are less accurate. This has been noticed, with a difference in displacements of the church's key components deviating between 5% and 15%. It is worth mentioning that the shell elements model is significantly less computationally expensive, and it may be favourable for future evaluations depending on the accuracy requirements.

For the church, most cracks are at the openings and brickwork arches supporting the ceiling and roof and occur due to the structure's self-weight.

What are the most important modelling criteria for determining the crack-width in the structural response?
The most valuable output of the structural model was the crack development in the masonry. This is mainly influenced by the material properties of the brickwork, the soil-structure interaction and connectivity assumptions. Regarding the deformations, the church model is predominantly influenced by horizontal displacements. Of the horizontal displacements, only a projection along the West-East direction is obtainable using InSAR.

It is recommended to better approximate the soil-structure interaction, given its importance and that of the horizontal displacements to the church structure. This can be done by either modelling the soil using solid finite elements or estimating the soil subgrade reaction relating to embedded rigid foundations. With the latter suggestion, differences can be made between longitudinal and lateral stiffness, which likely results in a more accurate representation of the interaction.

References

[Altun et al., 2010] Altun, A. O., Yilmaz, I., and Yildirim, M. (2010). A short review on the surficial impacts of underground mining. *Scientific research and essays*, 5(21):3206–3212.

[Balageas et al., 2010] Balageas, D., Fritzen, C.-P., and Güemes, A. (2010). *Structural health monitoring*, volume 90. John Wiley & Sons.

[Chen et al., 2020] Chen, D., Chen, H., Zhang, W., Cao, C., Zhu, K., Yuan, X., and Du, Y. (2020). Characteristics of the residual surface deformation of multiple abandoned mined-out areas based on a field investigation and sbas-insar: A case study in jilin, china. *Remote Sensing*, 12(22):3752.

[Corsetti et al., 2018] Corsetti, M., Fossati, F., Manunta, M., and Marsella, M. (2018). Advanced sbas-dinsar technique for controlling large civil infrastructures: An application to the genzano di lucania dam. *Sensors*, 18(7):2371.

[Doody, 2022] Doody, D. (2022). Basics of space flight - solar system exploration: Nasa science. [Online; accessed 03-February-2022].

[Drougkas et al., 2020a] Drougkas, A., Verstrynge, E., Balen, K. V., Shimoni, M., Croonenborghs, T., Hayen, R., and Declercq, P.-Y. (2020a). Country-scale insar monitoring for settlement and uplift damage calculation in architectural heritage structures. *Structural Health Monitoring*.

[Drougkas et al., 2020b] Drougkas, A., Verstrynge, E., Van Balen, K., Shimoni, M., Croonenborghs, T., Hayen, R., and Declercq, P.-Y. (2020b). Country-scale insar monitoring for settlement and uplift damage calculation in architectural heritage structures. *Structural Health Monitoring*, page 1475921720942120.

[EM 1110-1-1904, 1904] EM 1110-1-1904 (1904). Engineering and design settlement analysis. Engineer manual, U.S. Army Corps of Engineers, Washington, DC.

[ESA, 2020] ESA (2020). Esa - types of orbits.

[Ferretti et al., 2001] Ferretti, A., Prati, C., and Rocca, F. (2001). Permanent scatterers in sar interferometry. *IEEE Transactions on Geoscience and Remote Sensing*, 39(1):8–20.

[Giardina et al., 2019] Giardina, G., Milillo, P., DeJong, M. J., Perissin, D., and Milillo, G. (2019). Evaluation of insar monitoring data for post-tunnelling settlement damage assessment. *Structural Control and Health Monitoring*, 26(2):e2285.

[Google, 2012] Google (2012). Henryka sławika. https://www.google.co.uk/maps/@49.9879952,18.6251463,3a,75y,96.61h,110.89t/data=!3m6!1e1!3m4!1sBMDRySjR6dXtKCH2sHAjMw!2e0!7i13312!8i6656. [Online; accessed 02-October-2020].

[Herndon et al., 2021] Herndon, K., Meyer, F., Flores, A., Cherrington, E., and Kucera, L. (2021). What is synthetic aperture radar?

[Institute, 2020] Institute, P. G. I. N. R. (2020). Państwowy instytut geologiczny - państwowy instytut badawczy. http://geologia.pgi.gov.pl/arcgis/apps/MapSeries/index.html?appid=8d14826a895641e2be10385ef3005b3c. [Online; accessed 02-October-2020].

[Oliver and Webster, 2014] Oliver, M. and Webster, R. (2014). A tutorial guide to geostatistics: Computing and modelling variograms and kriging. *Catena*, 113:56–69.

[Perissin, 2016] Perissin, D. (2016). Interferometric sar multitemporal processing: Techniques and applications. In *Multitemporal Remote Sensing*, pages 145–176. Springer.

[SARPROZ, 2021] SARPROZ (2021). Sarproz - the sar processing tool by periz. https://www.sarproz.com/. [Online; accessed 14-April-2021].

[Selvakumaran et al., 2020] Selvakumaran, S., Rossi, C., Marinoni, A., Webb, G., Bennetts, J., Barton, E., Plank, S., and Middleton, C. (2020). Combined insar and terrestrial structural monitoring of bridges. *IEEE Transactions on Geoscience and Remote Sensing*, 58(10):7141–7153.

[Wikipedia, 2020] Wikipedia (2020). Kopalnia Węgla Kamiennego Borynia — Wikipedia, the free encyclopedia. http://pl.wikipedia.org/w/index.php?title=Kopalnia%20W%C4%99gla%20Kamiennego%20Borynia&oldid=59740753. [Online; accessed 02-October-2020].

[Yang et al., 2016] Yang, K., Yan, L., Huang, G., Chen, C., and Wu, Z. (2016). Monitoring building deformation with insar: Experiments and validation. *Sensors*, 16(12):2182.